TOWARDS UNCERTAINTY QUANTIFICATION OF PREMIXED LAMINAR FLAMES USING BAYESIAN STATISTICS

by

Dhruvin Jasmin Naik

December 10, 2015

A thesis submitted to the
Faculty of the Graduate School of the
State University of New York at Buffalo
in partial fulfillment of the requirements for the degree of

Master of Science

Department of Mechanical and Aerospace Department

Acknowledgements

These are my acknowledgements

Contents

List of Figures

List of Tables

Abstract

This is my abstract

Chapter 1

Introduction

It is important to understand deeply the dynamics of reacting flows as it is inherent in number of areas of science and engineering like combustion, surface chemistry etc . To understand these systems in detail, large simulations are necessary. It also requires simultaneous numerical resolution of chemical reactions, diffusive transport and fluid mechanics. The combination of three factor make simulations some of the most demanding in the area of combustion. In the deflagration (combustion wave that propagates through a gas or across the surface of an explosive at subsonic speeds, driven by the transfer of heat) regime where the burning speed (also known as laminar flame speed) and associated velocity scales are much smaller than the speed of sound in the fluid, the problem is acute.

For low speed combustion flows, Low Mach number asysmptotics of the flow equations exploit the inherent separation of scales in such systems by analytically eliminating acoustic wave propagation entirely from the dynamics, while preserving the important compressibility effects arising from reactions and transport.

1.1 Literature Review

It is shown by Muller that a multiple-time scale, single-space scale asymptotic analysis of the compressible Navier-Stokes equations reveals that the zeroth-order global thermodynamic pressure, the divergence of velocity and the material change of density are affected by heat-release rate and heat conduction at low-Mach-numbers.

His result show that the acoustic time change of the heat-release rate as the dominant source of sound in low-Mach-number flow. The asymptotic expansion of all flow variables show that the viscous and buoyancy forces enter the computation of the second-order incompressible pressure in low-Mach-number flow in a similar way as they enter the pressure computation in incompressible flow, except that the velocity-divergence constraint is non zero. He averaged flow equation over an acoustic wave period, the averaged velocity tensor described the net acoustic effect on the averaged flow field. Once acoustics were removed from the equations altogether it lead to the low-Mach-number equations.

As many flows of interest can be considered as incompressible. The incompressibility assumption makes the problem simpler than if a full compressible flow is considered. Codine proposed that for ideal fluids, with isentropic condition, solutions of the incompressible Navier Stokes equations can be found as the limit of solutions of the compressible ones as the Mach number tends to zero under certain assumptions on the initial data.
In her paper she showed that small Mach number limit gives rise to a separation of the pressure into a constant-in-space thermodynamic pressure and a mechanical pressure that has to be used in

the momentum equation. This leads to a removal of the acoustic modes and the flow behaves as incompressible, in the sense that the mechanical pressure is determined by the mass conservation equation and not by the state equation. However, large variations of density due to temperature variations are allowed. She showed that when the Mach number is small the hyperbolic wave equation for the pressure becomes an elliptic equation for the first order pressure p(2), thus showing the implicit (incompressible or mechanical) character of this pressure component

A.G Streng and A.V. Grosse studied the ozone oxygen flame experimentally. The stability of ozone and the rates of decomposition or explosion were investigated by Armour research foundation. Ozone was burned to oxygen from a simple burner tip in the range from 17 percent to 100 percent initial concentration of ozone in the mixture. The flame temperatures were calculated from enthalpy data and dissociation constants of oxygen using kelley's tables. The concentration of ozone was kept constant with error of 0.2 percent. Two methods were used to determine burning velocity i.e open tube method and the burning tip method. We will be using experimental burning velocity of the burning tip method. The burner tip experiments were carried out in standard apparatus, using pyrex glass aluminium tips with an inner diameter of 3 to 0.65mm. The flames were readily observed by the standard schlieren method at all concentrations above 30 mole percent. The measurements were all carried out in the laminar flow region and the reynolds number of the flow was below 2000. The initial conditions are 300K temperature and 1.0 atmosphere pressure. The results of burning velocities of ozone flames were compared with theoretical burning velocities of Dr. Von Karman and his associates. They were found to be in close agreements.

Chapter 2

Mathematical Model

2.1 Governing Equations

Need transition description (will write later)

2.1.1 Problem definition

The flow of a compressible fluid is described in terms of the velocity (u^*), pressure (p^*), density (ρ^*), and temperature(T^*) fields. These fields are solutions of the compressible Navier Stokes equations that describe the dynamics of the system and that are statements of conservation of mass, momentum and energy and a state equation relating the thermodynamic variables.

The system of equation that needs to be solved reads

$$\frac{D\rho^*}{Dt^*} = -\rho^* \nabla \cdot u^* \tag{2.1}$$

$$\rho^* \frac{Du^*}{Dt} = -\nabla p^* + \nabla \cdot \tau^* + \rho^* g^* \tag{2.2}$$

$$\rho^* C_p^* \frac{DT^*}{Dt^*} = \tau^* \nabla \cdot u^* - \nabla \cdot q^* + \beta^* T^* \frac{Dp^*}{Dt^*} \tag{2.3}$$

$$\frac{D\rho^*}{Dt^*} = -\beta^* T^* \frac{D\rho^*}{Dt^*} + \alpha^* \rho^* \frac{Dp^*}{Dt^*} \tag{2.4}$$

Where u^* is the velocity vector,ρ^* is the density,β^* is the thermal expansion coefficient,p^* is the pressure ,τ^* is the viscous stress term, g^* is the gravitational vector,c_p^* is the specific heat, T^* is the temperature, q^* is the heat flux vector.

for Newtonian fluid,

$$\tau^* = \mu^*(\nabla u^* + (\nabla u^*)^T)) - \frac{2}{3}\mu^* \nabla \cdot u^* I$$

By fourier law's,

$$q^* = k^* \nabla T^*$$

μ^* is the dynamic viscocity. k^* is the thermal conductivity.

The following are the quantities in equation of state, $\beta^* = -\frac{1}{\rho^*}\frac{\partial \rho^*}{\partial T^*}$ and $\alpha^* = \frac{1}{\rho^*}\frac{\partial \rho^*}{\partial p^*}$.

2.1.2 Low mach number asymtotic analysis

We nondimensionalize the Equations by using reference quantities denoted by the subscript ∞, e.g. farfield or stagnation conditions, and a typical length scale L^* of the considered flow. The thermodynamic reference quantities are assumed to be related by the equation of state for a perfect gas. We have used perfect gas law because we are dealing with gases in combustion environment. We define the nondimensional quantities by:

$$\rho = \frac{\rho^*}{\rho_\infty},\ p = \frac{p^*}{p_\infty},\ u = \frac{u^*}{u_\infty},\ T = \frac{T^*}{T_\infty},\ \mu = \frac{\mu^*}{\mu_\infty},\ k = \frac{k^*}{k_\infty}, x = \frac{x^*}{L^*},\ t = \frac{t^*}{L^*/u^*_\infty},\ \beta^* = \frac{\beta}{\beta_\infty},$$

$C_p^* = \frac{C_p}{C_{p^*_\infty}}$.

Using the relations above. we may write the nondimensional Navier-Stokes equations and other equations of interest as follows:

$$\frac{D\rho}{Dt} = -\rho\,\nabla\cdot u \tag{2.5}$$

$$\rho\frac{Du}{Dt} = -\frac{1}{M^2}\,\nabla p + \frac{1}{Re}\nabla\cdot\tau + \frac{1}{Fr^2}\rho g \tag{2.6}$$

$$\rho C_p\frac{DT}{Dt} = \frac{M^2}{Re\lambda}\,\tau\nabla\cdot u - \frac{1}{RePr}\,\nabla\cdot(k\nabla T) + \frac{\beta T}{\lambda}\frac{Dp}{Dt} \tag{2.7}$$

$$\frac{D\rho}{Dt} = -\beta T\frac{D\rho}{Dt} + \alpha\rho\,\frac{Dp}{Dt} \tag{2.8}$$

Where the following nondimensional quantities are

$$M = \frac{u_\infty}{a_\infty}$$

.

$$Re = \frac{u_\infty\rho_\infty L}{\mu_\infty}$$

.

$$Pr = \frac{C_{p_\infty}\mu_\infty L}{k_\infty}$$

$$Fr = \sqrt{\frac{u^2_\infty}{g_\infty L}}$$

.

a_∞ is the reference speed of sound. M is the mach number,Re is the reynolds number,Pr is the prandtl number,Fr is the froude number and λ is defined as $\frac{C_{p_\infty}T_\infty}{a^2_\infty}$.
By definition

$$\beta^* = -\frac{1}{\rho^*}\frac{\partial\rho^*}{\partial T^*}$$

We non dimensional this term as follows

$$\beta^* = -\frac{1}{\rho_\infty\rho}\frac{\rho_\infty}{T_\infty}\frac{\partial\rho}{\partial T}$$

$$\beta^* = \frac{1}{T_\infty}\beta$$

Where $\beta_\infty = \frac{1}{T_\infty}$.

By definition

$$a^{*2} = \frac{\partial p^*}{\partial \rho^*}$$

We non dimensional this term as follows

$$a^{*2} = \frac{p_\infty}{\rho_\infty}\frac{\partial p}{\partial \rho}$$

$$a^{*2} = \frac{p_\infty}{\rho_\infty}a^2$$

Where $a_\infty = \sqrt{\frac{p_\infty}{\rho_\infty}}$.

2.1.3 Asymptotic analysis

We do asymptotic analysis with respect to Mach number. We use the following equation in terms of Mach number

$$\xi(x,t,M) = \xi^0(x,t) + M\xi^1(x,t) + M^2\xi^2(x,t) + O(M^3)$$

Where ξ can be u, p, ρ. We use non dimensional form of navier stokes equation do the asymptotic equation. We show the example of asymptotic analysis for mass conservation.

$$\frac{D}{Dt}(\rho^0 + M\rho^1 + M^2\rho^2 + O(M^3)) \; + \; (\rho^0 + M\rho^1 + M^2\rho^2 + O(M^3)) \; \nabla\cdot(u^0 + Mu^1 + M^2u^2 + O(M^3)) = 0$$

Collecting equal order terms together we get,

$$\left(\frac{D\rho^0}{Dt} \; + \; \rho^0 \; \nabla\cdot u^0\right) + M\left(\frac{\partial \rho^1}{\partial t} + + \rho^1 \; \nabla\cdot u^0 + + \rho^0 \; \nabla\cdot u^1\right) + O(M^2) = 0$$

Therefore zeroth order terms can be written.

$$\frac{D\rho^0}{Dt} \; + \; \rho^0 \; \nabla\cdot u^0 \quad = \quad 0 \tag{2.9}$$

The asymptotic relation for momentum are obtained are as follows. The zero, first and second order momentum equation are written as follows respectively

$$M^{-2}\nabla p^{(0)} \quad = \quad 0 \tag{2.10}$$

$$M^{-1}\nabla p^{(1)} \quad = \quad 0 \tag{2.11}$$

$$\rho^0\frac{Du^0}{Dt} \quad = \quad -\nabla p^2 \; + \; \nabla\cdot\tau^0 + \rho^0 g \tag{2.12}$$

The asymptotic relation for momentum are obtained are as follows.

$$\rho^0 C_p^0\frac{DT^0}{Dt} \quad = \quad -\frac{1}{RePr}\,\nabla.(k^0\nabla T^0) + \frac{\beta^0 T^0}{\lambda}\frac{dp^0}{dt} \tag{2.13}$$

We have seen from momentum asymptotic analysis that $p^0 = p^0(t)$ and therefore

$$\frac{Dp^0}{Dt} = \frac{dp^0}{dt}$$

.
The nondimensional equation of state is same as that of the dimensional form. Now same asymptotic expansion of the state equation is done in order to get zeroth order state equation which is given below.

$$\frac{D\rho^0}{Dt} = -\beta^0 T^0 \frac{D\rho^0}{Dt} + \alpha^0 \rho^0 \frac{Dp^0}{Dt} \tag{2.14}$$

From mass conservation equation and since $p^0 = p^0(t)$, we get the following equation

$$-\nabla \cdot u^0 = -\beta^0 \frac{DT^0}{Dt} + \alpha^0 \frac{dp^0}{dt} \tag{2.15}$$

From energy conservation equation

$$-\rho^0 C_p^0 \nabla \cdot u^0 = \frac{1}{RePr} \nabla \cdot q^0 + \left(\frac{C_p^0 \lambda - 1}{\lambda} \right) \frac{dp^0}{dt} \tag{2.16}$$

The final equation obtained by applying various thermodynamic properties are following

$$-\nabla \cdot u = \frac{1}{p^0} \frac{dp^0}{dt} - \frac{1}{T} \frac{DT}{Dt} \tag{2.17}$$

$$\rho \frac{Du}{Dt} = -\frac{1}{M^2} \nabla p + \frac{1}{Re} \nabla \cdot \tau + \frac{1}{Fr^2} \rho g \tag{2.18}$$

$$\rho C_p \frac{DT}{Dt} = -\frac{1}{RePr} \nabla \cdot (k \nabla T) + \frac{1}{\gamma - 1} \frac{dp^0}{dt} \tag{2.19}$$

$$\tag{2.20}$$

Chapter 3

Combustion Model

3.1 Premixed ozone oxygen laminar flame model

We shall use Heimerl and coffee's contemporary method for modelling combustion flame problem. A one dimensional, premixed, laminar, steady state ozone oxygen flame was considered in their theortical model. The reason for choosing this model was due to its simplicity. The chemical reactions involved only three species

$$O_3 + M \rightleftharpoons O + O_2 + M$$

$$O + O_3 \rightleftharpoons A_2 2O_2$$

$$A + AB \rightleftharpoons A_2 + B$$

Where M represents the third body which could be either O, O_2 or O_3.
The species conservation equation is given as

$$\frac{\partial \rho_i}{\partial t} + \nabla.(\rho_i v) \quad = \nabla.(\rho D_{ij} \nabla Y_i) + w_i \tag{3.1}$$

Where, the rate of production for species i is given by the following
Where

$$w_i = M w_i \sum_{k=1}^{6} (v_{k,i}^{''} - v_{k,i}^{'}) B_k T^{\alpha_k} e^{\frac{-E_a}{R_u T}} \prod_{j=1}^{3} \left(\frac{X_j p}{RT} \right)^{v_{j,k}^{'}}$$

The above equation considers all 6 reactions for all the three species.
From atomic species conservation

$$\sum_{i=1}^{N} v_i{}' M_i \rightleftharpoons \sum_{i=1}^{N} v_i{}'' M_i$$

Where E_a is the activation energy, R_u is the universal gas constant, X_j is the molar concentration of the reactant j, Mw_i is the molecular weight of the reactant. $v_{j,k}^{'}$ is the moles of reactant j in the reaction k. $v_{j,k}^{''}$ is the number of moles of product.

The overall continuity equation, species conservation equation and energy conservation equation are solved to calculate the flame parameters. The energy equation considers that the pressure is constant throughout the reaction zone. The viscous dissipation is negligible and there is no body force work.

The Diffusion equation is given

$$\frac{\partial X_k}{\partial x} = \sum_{j=1}^{3} \frac{X_k X_j}{D_{jk}} (V_j - V_k) \tag{3.2}$$

Where D_{jk} is the fick's diffusion coefficient. V is the diffusion velocities.
The boundaries are defined by specifying the concentration of O_3, O_2 at the inlet.

3.2 The experimental data on laminar flame speed

To compare our results we have used the experimental data given by the A.G. streng and A.V. Grosse, They have done experiments with ozone flame in tube and ozone flame on the tip of the burner. We will be using the results of the later. They have shown that laminar flame speed or burning velocity varies with the initial concentration of the ozone. The table given below shows the burning velocity with respect to initial concentration of the ozone. We concentrate on two speciifc cases where initial concentration of ozone is 53 percent and 100 percent. The laminar flame speed for 53 percent is measured in the burner with inner diameter 1.3mm and rate of 7.7 cc/sec. The laminar flame speed for 100 percent ozone is taken on .66 inner diameter tip 0.66 mm and the flow rate of 8.23 cc/sec. The measured laminar flame speed is given below. Laminar flame measurements are carried out at 300K and 1 atmosphere pressure.

Table 3.1: Experimental laminar flame speed given by A.G. Streng and A.V. Grosse

Initial Concentration of O_3 ($\pm 0.2\%$)	**Laminar Flame Speed (cm/s)**
17	9.2
20	18.2
28	52.2
40	125
46	166
53	210
75	331
100	475

3.3 Geometry with boundary conditions

- AB is the inlet
- BC is the thickness of the burner tube
- CD is the outside of the burner
- DE, EF is the domain of interest
- AE is the Axisymmetric line

The following assumption are made

- At the inlet, the incoming velcity has parabolic profile. i.e poissuelle flow.
- The surface chemistry at the wall of the burner is neglected.

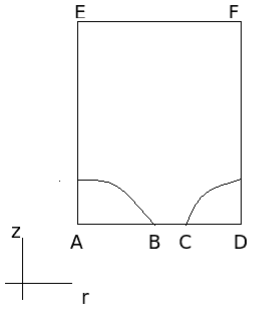

Figure 3.1: Geometry

- At the outside of the burner, the incoming air has couette flow profile.
- DE, EF are the boundaries of the domain. No change occurs after this point.

The boundary conditions are defined as follows

At the inlet (AB)

- $u_r = 0$ and $u_z = 5801.9mm/s$
- $C_i = 1$
- $T = 300K$
- $p = 1atmos$

On BC

- $u_r = 0$ and $u_z = 0mm/s$
- $\frac{\partial C_i}{\partial r} = 0$ and $\frac{\partial C_i}{\partial z} = 0$
- $T = 300K$
- $p = 1atmos$

On CD

- $u_r = 0$ and $u_z = 5801.9mm/s$
- $C_{O_2} = 21\%$
- $T = 300K$
- $p = 1atmos$

On DF and FE

- $\frac{\partial u_r}{\partial r} = 0$ and $\frac{\partial u_z}{\partial z} = 0$
- $\frac{\partial C_i}{\partial r} = 0$ and $\frac{\partial C_i}{\partial z} = 0$
- $\frac{\partial T}{\partial r} = 0$ and $\frac{\partial T}{\partial z} = 0$

- $\frac{\partial p}{\partial r} = 0$ and $\frac{\partial p}{\partial z} = 0$

On AF

- $\frac{\partial u_r}{\partial r} = 0$
- $\frac{\partial C_i}{\partial r} = 0$
- $\frac{\partial T}{\partial r} = 0$
- $\frac{\partial p}{\partial r} = 0$

3.4 Transport Model

3.4.1 Viscocity

We have used viscosity model as derived from kinetics theory under the ideal gas assumption The kinetic theory uses the assumption of the ideal gas law.

$$pv = nRT$$

Where p is the pressure, v is the volume, n is the number of moles of the gas, R is the universal gas constant and T is the temperature. The viscocity of the species is given by the following formula

$$\eta_s = \frac{5}{16}\sqrt{\frac{m_s k_B T}{\pi}}\frac{f_n}{{\sigma_s}^2 \Omega^{(2,2^*)}}$$

Where m the molecular mass of the species (kg), σ is the Lennard-Jones potential diameter associated to the species (m), k_B is the Boltzmann constant,$\Omega^{(2,2^*)}$ is the value of the dimensionless integrated integral from Monchick and Mason (1961). With hard sphere approximation $f_n = 1$. We have three species in our system i.e O, O_2 and O_3. We have varied temperature from 300 K to 2700 K and plotted the viscocity V/s Temperature for all the three species. The σ values and constants for dimensionless collision number are taken from NASA CAE transport file.

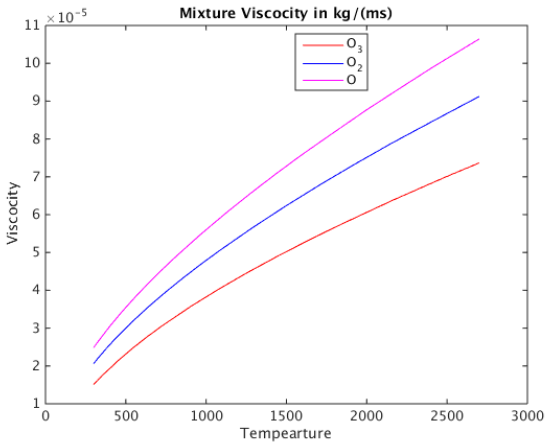

model.png

Figure 3.2: Viscocity

3.4.2 Bimolecular Diffusion

The molecular binary diffusion model is computed from kinetics theory, assuming the ideal gas hypothesis. The molecular binary diffusion coefficient ($m^2 s^{-1}$) is given by:

$$D_{ij} = \frac{3}{16}\sqrt{\frac{2k_B^3 T^3}{\pi m_{ij}}}\frac{f_n}{P{\sigma_{ij}}^2 \Omega^{(1,1^*)}}$$

with the reduced mass

$$m_{ij} = \begin{cases} \frac{m_i m_j}{m_i + m_j} & i \neq j \\ m_i & i = j \end{cases} \tag{3.3}$$

σ_{ij} is the Lennard-Jones collision diameter between species i and j:

$$\sigma_{ij} = \frac{1}{2}\left(\sigma_i + \sigma_j\right)\xi^{-\frac{1}{6}} \tag{3.4}$$

and $\Omega^{(1,1^*)}$ the integrated collision interval, fitted from the tables given in Monchick and Mason(1961). We have varied temperature from 300 K to 2700 K and plotted the Diffusion coefficient V/s Temperature for all the combination of three species. The σ values and constants for dimensionless collision number are taken from NASA CAE transport file.

3.4.3 Species Thermal Conductivity

The thermal conduction of a species i is given by

$$\begin{aligned} \lambda_i &= \lambda_i^{(\text{rot})} + \lambda_i^{(\text{trans})} + \lambda_i^{(\text{vib})} \\ \lambda_i &= \frac{\eta_i}{M_i}\left(C_{v,i}^{(\text{trans})}\lambda_i^{(\text{trans})} + C_{v,i}^{(\text{rot})}\lambda_i^{(\text{rot})} + C_{v,i}^{(\text{vib})}\lambda_i^{(\text{vib})}\right) \end{aligned}$$

with

$$\begin{aligned} \lambda_{v,i}^{(\text{vib})} &= \rho_i \frac{D_{i,i}}{\eta_i} \\ \lambda_{v,i}^{(\text{rot})} &= \rho_i \frac{D_{i,i}}{\eta_i}\left(1 + \frac{2}{\pi}\frac{A}{B}\right) \\ \lambda_{v,i}^{(\text{trans})} &= \frac{5}{2}\left(1 - \frac{2}{\pi}\frac{C_{v,i}^{(\text{rot})}}{C_{v,i}^{(\text{trans})}}\frac{A}{B}\right) \end{aligned}$$

and

$$\begin{aligned} A &= \frac{5}{2} - \rho_i \frac{D_{i,i}}{\eta_i} \\ B &= Z_{rot} + \frac{2}{\pi}\left(\frac{5}{3}\frac{C_{v,i}^{(\text{rot})}}{R} + \rho_i \frac{D_{i,i}}{\eta_i}\right) \end{aligned}$$

the rotational relaxation number is given by

$$Z_{rot,i}(T) = Z_{rot,i}(298)\frac{F(298)}{F(T)} \tag{3.5}$$

with the function F defined as

$$F(T) = 1 + \frac{\pi^{\frac{3}{2}}}{2}\sqrt{\left(\frac{\epsilon_i}{k_B T}\right)} + \left(\frac{\pi^2}{4} + 2\right)\left(\frac{\epsilon_i}{k_B T}\right) + \pi^{\frac{3}{2}}\left(\frac{\epsilon_i}{k_B T}\right)^{\frac{3}{2}} \tag{3.6}$$

The specific heat are given by the thermodynamic module. We have varied temperature from 300 K to 2700 K and plotted the thermal conductivity V/s Temperature for all the three species. The σ values and constants for dimensionless collision number are taken from NASA CAE transport file.

3.4.4 Mixture Model

The Wilke formula for viscosity, independent of the viscocity model, is

$$\eta_{\text{mixture}} = \sum_{s=1}^{n} \frac{x_i \eta_i}{\sum_{j=1}^{n} x_j \Phi_{ij}} \tag{3.7}$$

with

$$\Phi_{ij} = \frac{\left[1 + \sqrt{\frac{\eta_i}{\eta_j}\sqrt{\frac{M_j}{M_i}}}\right]^2}{\sqrt{8\left(1 + \frac{M_i}{M_j}\right)}} \tag{3.8}$$

We have varied temperature from 300 K to 2700 K and plotted the mixture viscocity V/s Temperature for all the three species. The σ values and constants for dimensionless collision number are taken from NASA CAE transport file. We have considered three cases- behind the flame where condentration of O_3,O_2 and O are taken to be .53, .47 and 0 respectively. Second case of the inside of the flame where concentrations are 0.5, 0.4 and 0.1 respectively. The third case is of the behind the flame where ozone and oxygen radical are absent and there will be only O_2
For the bimolecular diffusion model, we use:

$$D_i = \frac{1 - y_i}{\sum_{j \neq i}^{n} \frac{x_i}{D_{ji}}} = \frac{\sum_{j \neq i}^{n} x_j M_j}{M_{\text{mixture}} \sum_{j \neq i}^{n} \frac{x_j}{D_{ji}}} \tag{3.9}$$

The thermal conductivity of the mixture is given by

$$\lambda_{\text{mixture}} = \sum_{s=1}^{n} \frac{x_i \lambda_i}{\sum_{j=1}^{n} x_j \Phi_{ij}} \tag{3.10}$$

We have varied temperature from 300 K to 2700 K and plotted the mixture thermal conductivity V/s Temperature for all the three species. The σ values and constants for dimensionless collision number are taken from NASA CAE transport file. We have considered three cases- behind the flame where condentration of O_3,O_2 and O are taken to be .53, .47 and 0 respectively. Second case of the inside of the flame where concentrations are 0.5, 0.4 and 0.1 respectively. The third case is of the behind the flame where ozone and oxygen radical are absent and there will be only O_2

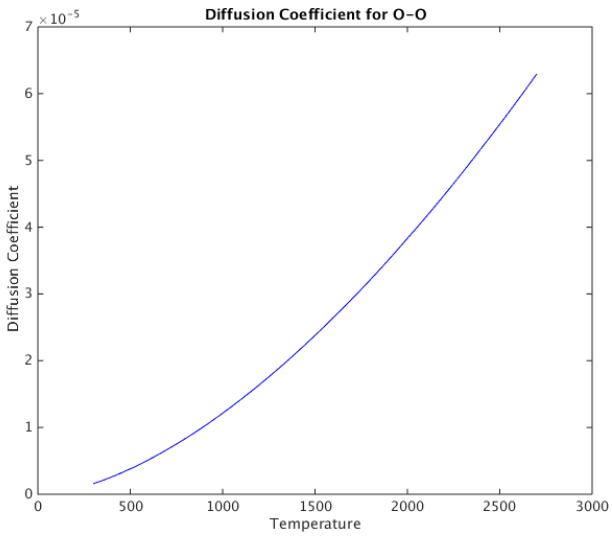

(a) Diffusion coefficient for O - O

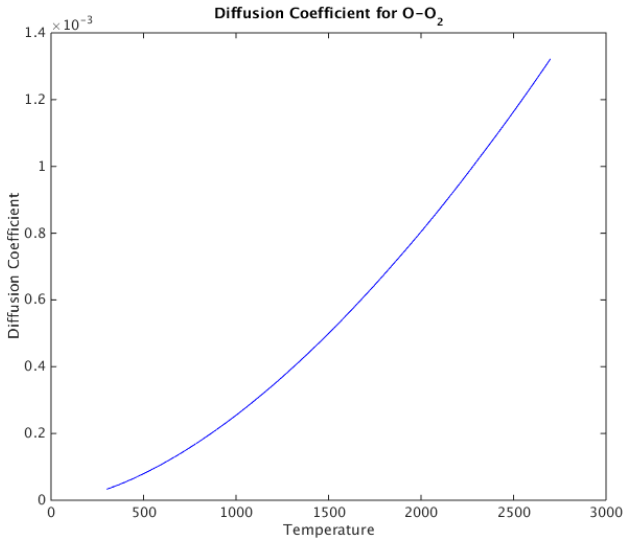

(b) Diffusion coefficient for O - O_2

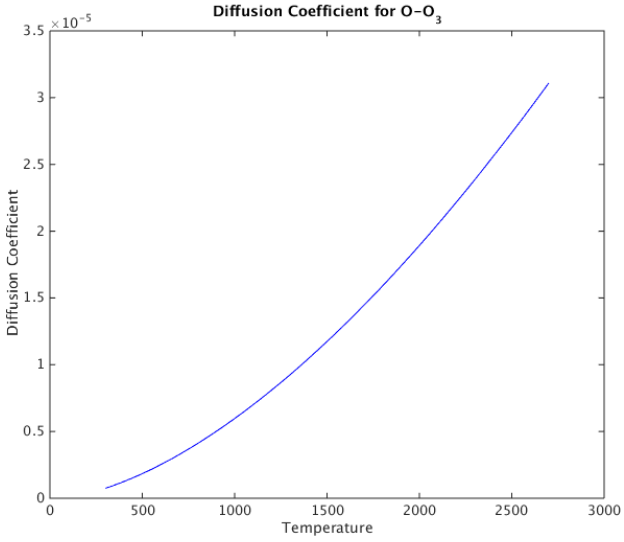

(c) Diffusion coefficient for O - O_3

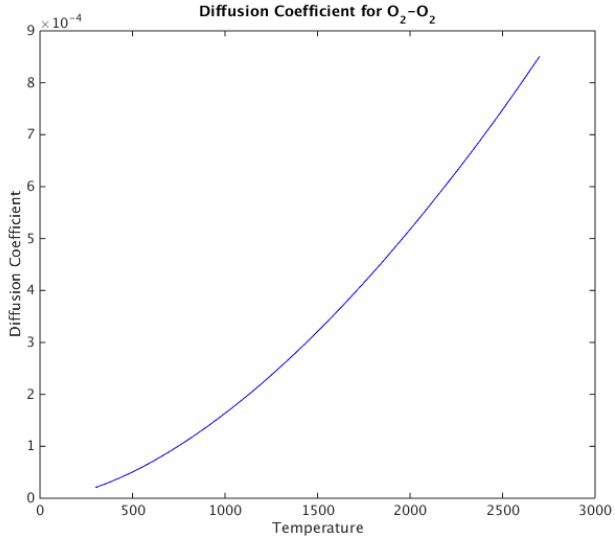

(d) Diffusion coefficient for O_2 - O_2

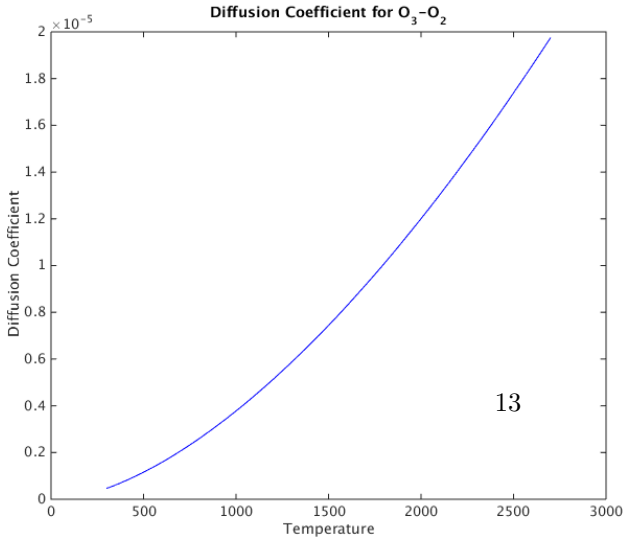

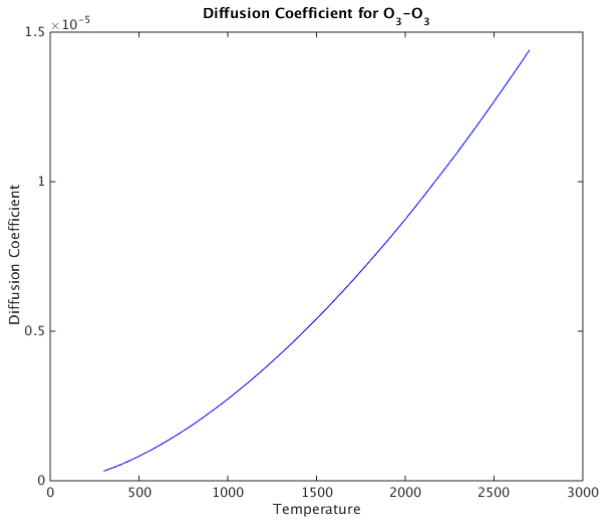

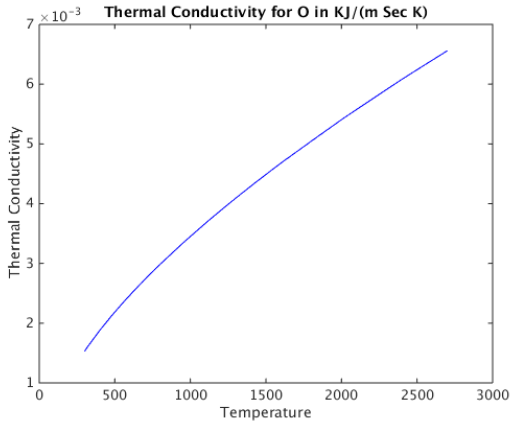

(a) Thermal Conductivity for O

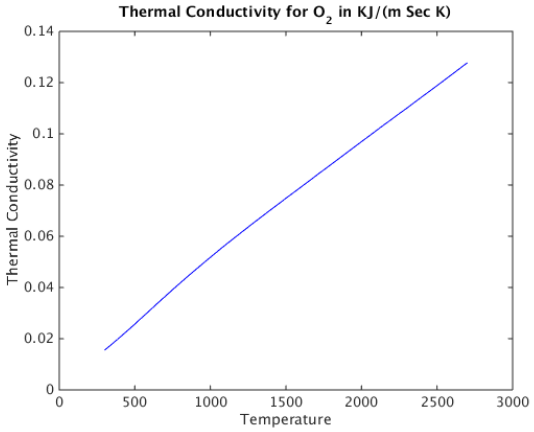

(b) Thermal Conductivity for O_2

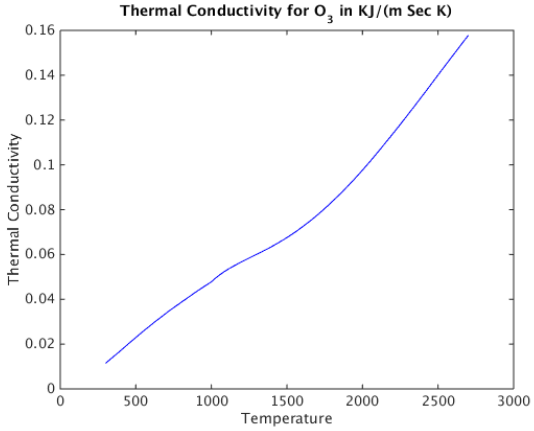

(c) Thermal Conductivity for O_3

Figure 3.4: Thermal Conductivity

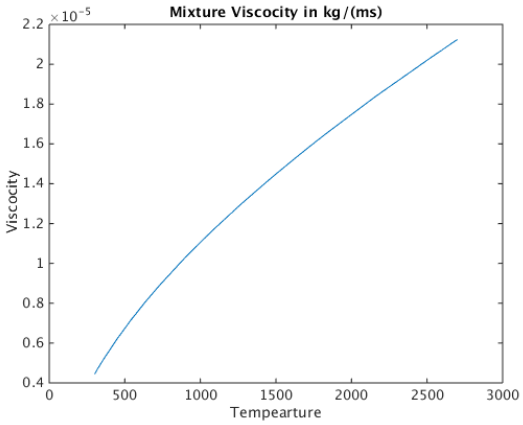

(a) Mixture Viscocity behind the flame

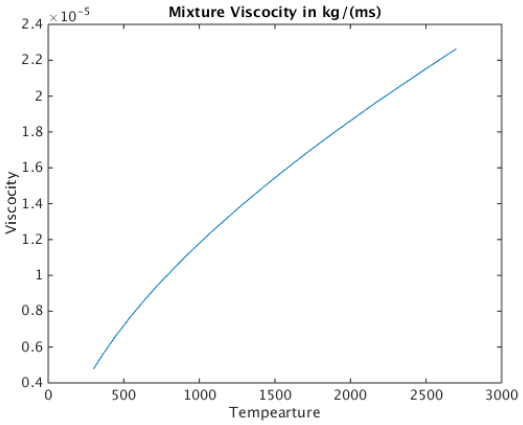

(b) Mixture Viscocity inside the flame

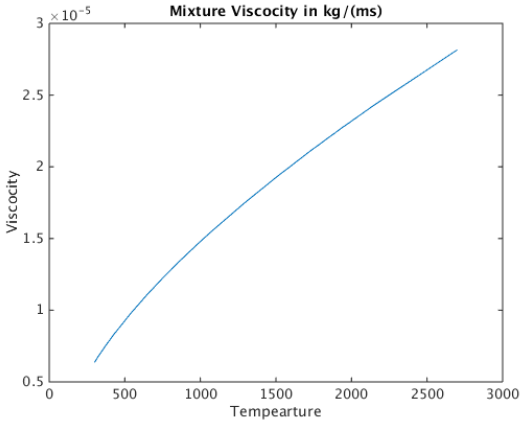

(c) Mixture Viscocity after the flame

Figure 3.5: Mixture Viscocity

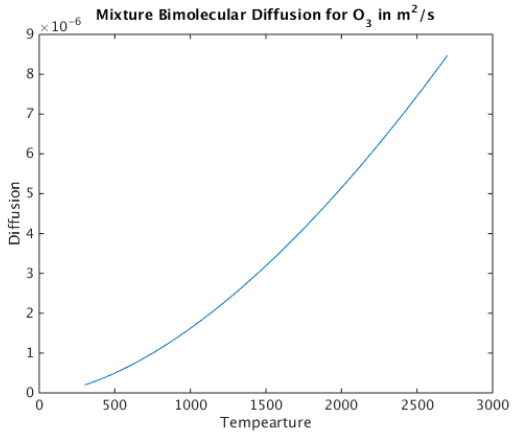

(a) Mixture Diffusion coefficient for O_3 behind the flame

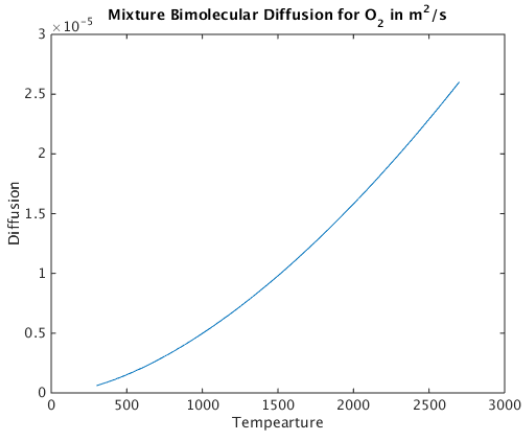

(b) Mixture Diffusion coefficient for O_2 behind the flame

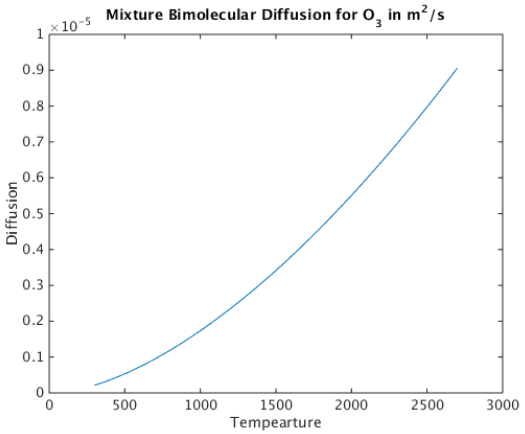

(c) Mixture Diffusion coefficient for O_3 inside the flame

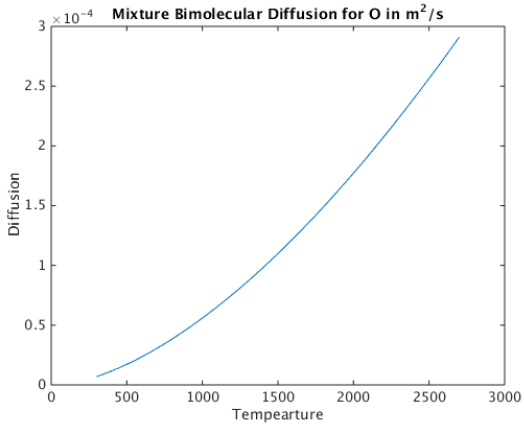

(d) Mixture Diffusion coefficient for O inside the flame

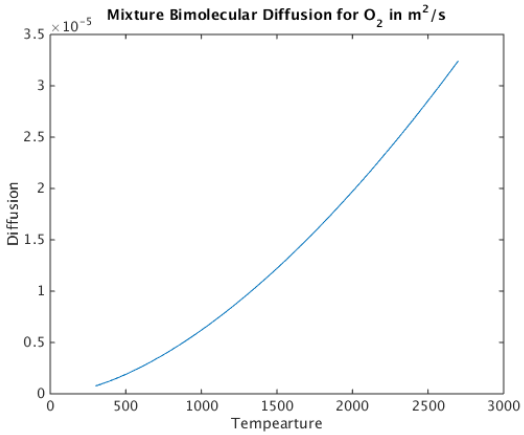

(e) Mixture Diffusion coefficient for O_2 inside the flame - O_3

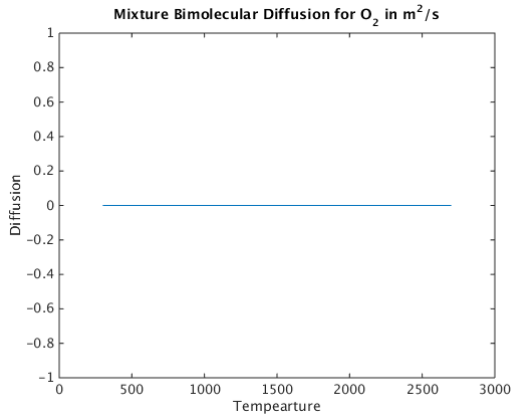

(f) Mixture Diffusion coefficient for O_2 after the flame - O_3

Figure 3.6: Mixture Diffusion coefficient

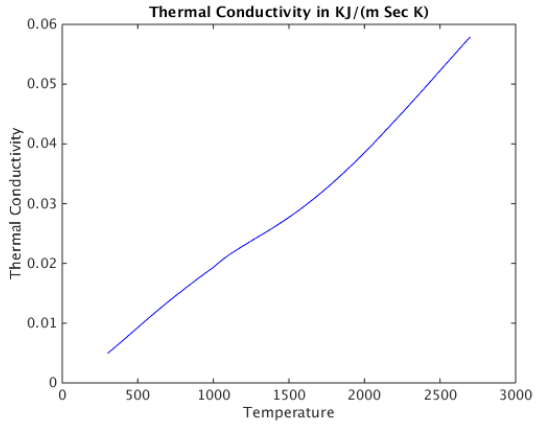

(a) Mixture thermal conductivity behind the flame

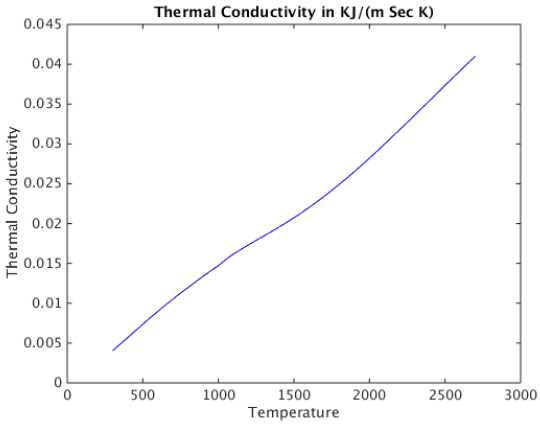

(b) Mixture thermal conductivity inside the flame

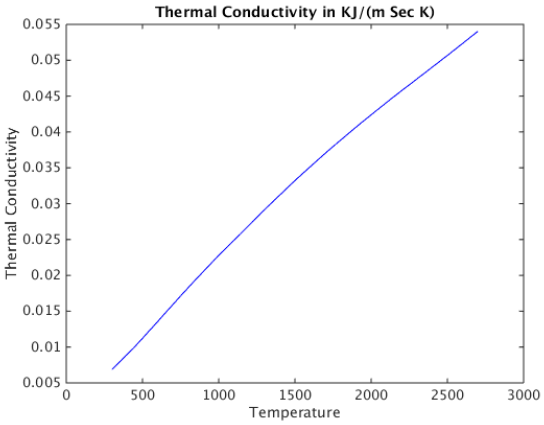

(c) Mixture thermal conductivity after the flame

Figure 3.7: Mixture thermal conductivity

Chapter 4

Finite Element Formulation

4.1 Weak formulation

The final equation obtained by applying various thermodynamic properties are following

$$-\nabla \cdot u = \frac{1}{p^0}\frac{dp^0}{dt} - \frac{1}{T}\frac{DT}{Dt} \tag{4.1}$$

$$\rho\frac{Du}{Dt} = -\frac{1}{M^2}\nabla p + \frac{1}{Re}\nabla \cdot (\mu(\nabla u + (\nabla u)^T) - \frac{2}{3}\mu\nabla \cdot uI) + \frac{1}{Fr^2}\rho g \tag{4.2}$$

$$\rho C_p\frac{DT}{Dt} = -\frac{1}{RePr}\nabla \cdot (k\nabla T) + \frac{1}{\gamma - 1}\frac{dp^0}{dt} \tag{4.3}$$

$$\tag{4.4}$$

The 2D finite element weak form is given as

$$\int_0^L\int_0^L \rho\frac{\partial u^h}{\partial t}\psi + \int_0^L\int_0^L (\rho u^h \cdot \nabla u^h)\psi = \int_0^L\int_0^L -\frac{1}{M^2}(\nabla p^h)\phi + \int_0^L\int_0^L \frac{1}{Re}(\nabla \cdot \tau^h)\psi + \int_0^L\int_0^L \frac{1}{Fr^2}(\rho g)\psi$$

$$\int_0^L\int_0^L \rho C_p\frac{\partial T^h}{\partial t}\varphi + \int_0^L\int_0^L \rho C_p(u^h \cdot \nabla T^h)\varphi = \int_0^L\int_0^L -\frac{1}{RePr}(\nabla \cdot k\nabla T^h)\varphi + \int_0^L\int_0^L \frac{1}{\gamma - 1}\frac{dp^h}{dt}\phi$$

Integrating by parts and applying boundary conditions

$$\int_0^L\int_0^L \rho\dot{u}^h\psi_i\psi_j + \int_0^L\int_0^L \rho u^h \cdot \nabla u^h\psi_i = \int_0^L\int_0^L -\frac{1}{M^2}\nabla p^h\phi_i - \int_0^L\int_0^L \frac{1}{Re}\tau^h\nabla\psi + [\tau\psi]_0^L + \int_0^L\int_0^L \frac{1}{Fr^2}\rho g\psi$$

$$\int_0^L\int_0^L \rho C_p\dot{T}^h\varphi_i\varphi_j + \int_0^L\int_0^L \rho C_p u^h \cdot \nabla T\varphi_i = \int_0^L\int_0^L +\frac{1}{RePr}(k\nabla T^h)\nabla\varphi - \frac{1}{RePr}\left[k\nabla T^h\varphi\right]_0^L + \int_0^L\int_0^L \frac{1}{\gamma - 1}\frac{dp^h}{dt}\phi$$

4.2 Need for stability

Using numerical methods in a straightforward way for the approximation of arbitrary differential equations may cause severe problems. There are Oscillations, locking, singular matrices and other problems in the result in certain concrete problem. Thus, stabilization is needed. To obtain satisfactory approximations stabilization may be needed. The matrix of the advective term is non-symmetric (non-self adjointness of the convective operator) and the best approximation property is lost . As a result Bubnov-Galerkin methods applied to these problems are far from optimal and show spurious oscillations in the solutions, worsening with growing convection-domination.
To characterize the relative importance of convective and diffusive effects in a given flow problem, it is useful to introduce the mesh Peclet number.

$$Pe = \frac{ah}{2\nu}$$

which expresses the ratio of convective to diffusive transport. The Galerkin solution is corrupted by non-physical oscillations when the Peclet number is larger than one. The Galerkin method loses its best approximation property when the non-symmetric convection operator dominates the diffusion operator in the transport equation, and consequently spurious node-to-node oscillations appear.
All stabilization schemes applied are Petrov-Galerkin approaches. They all add perturbations to the original Bubnov-Galerkin weak form. These perturbations are formulated in terms of modifications of the Bubnov-Galerkin test functions. They are multiplied with the residuals of the differential equations and thereby ensure consistency. Additionally, a stabilization parameter ξ weights the influence of the added stabilization terms.

4.2.1 Streamline Upwind Petrov Galerkin Method

To ensure that the solution of the differential equation is also a solution of the weak form, it is necessary to stabilize the convective term in a consistent manner. To accomplish this an extra term over the element interiors is added to the Galerkin weak form. This term has to be a function of the residual of the differential equation or else the equation will not be consistent. It introduces a certain amount of artificial diffusion in streamline direction only. The latter aspect ensures that no diffusion perpendicular to the flow direction is introduced, which was the reason for excessive over diffusion in other methods.

Stabilization through a product of a perturbation and the residual is a fundamental aspect of successful stabilization schemes and is realized in all stabilization method applied here. The following term is added to the galerkin weak form of the differential equation.

$$\sum_e \int_{\Omega^e} P(w)\xi R(u) d\Omega$$

Where $P(w)$ is a certain operator applied to the test function, ξ is the stabilization parameter (also called intrinsic time), and $R(u)$ is the residual of the differential equation. The stabilization techniques are characterized by the definition of $P(w)$

The SUPG stabilization technique is defined by taking

$$P(w) = a.\nabla w$$

where a is the convection velocity. w is the test function. This corresponds to the perturbation of the test function. The space of the test functions does not coincide with the space of the interpolation functions, hence it is called as PetrovGalerkin formulation.

For simple convection diffusion equation $\tau = \frac{\overrightarrow{\nu}}{||a||^2}$. For 1D $\overrightarrow{\nu} = \frac{\beta a h}{2}$ and $\beta = coth(Pe) - \frac{1}{Pe}$

4.2.2 Pressure-Stabilizing/Petrov-Galerkin (PSPG)

In mixed convection-dominated problems, such as the incompressible Navier-Stokes equations with high Reynolds-numbers, SUPG and PSPG (called herein SUPG/PSPG) stabilization have to be applied to obtain satisfactory results. It should also be mentioned that the PSPG stabilization parameter does not necessarily have to be identical with the SUPG stabilization parameter

The terms associated with parameter ξ_{pspg} (pressure-stabilizing/Petrov-Galerkin) allow the use of mixed elements with equal-order interpolations for the velocity and pressure. All stabilization terms are weighted residuals, therefore ensuring the consistency of the formulation. The following term is added to the galerkin weak form of the differential equation.

$$\sum_e \int_{\Omega^e} \nabla\phi \xi_{pspg} R(u) d\Omega$$

4.2.3 Stabilized Navier Stokes Equation

From the stabilization discussions we can now write the stabilized form of Navier stokes equation. The Residual of momentum and energy equation are given as follows

$$\begin{aligned} R1(u) &= \rho\frac{Du^h}{Dt} + \frac{1}{M^2}\nabla p^h - \frac{1}{Re}\nabla\cdot(\mu^*(\nabla u^h + (\nabla u^h)^T) - \frac{2}{3}\mu^h\nabla\cdot u^h I) - \frac{1}{Fr^2}\rho g \\ R2(T) &= \rho C_p\frac{DT^h}{Dt} + \frac{1}{RePr}\nabla\cdot(k\nabla T^h) - \frac{1}{\gamma-1}\frac{dp^h}{dt} \end{aligned}$$

Now adding the pressure stabilization and convection stabilization to momentum and energy equations we get the following expressions

$$\begin{aligned} \int_0^L\int_0^L \rho\dot{u}^h\psi_i\psi_j + \int_0^L\int_0^L \rho u^h\cdot\nabla u^h\psi_i + \int_0^L\int_0^L \frac{1}{M^2}\nabla p^h\phi_i + \int_0^L\int_0^L \frac{1}{Re}\tau^h\nabla\psi + \\ -\int_0^L\int_0^L \frac{1}{Fr^2}\rho g\psi + \sum_e\int_{\Omega^e} P(\psi)\xi R1(u)d\Omega + \sum_e\int_{\Omega^e}\nabla\phi\xi_{pspg}R1(u)d\Omega &= [\tau\psi]_0^L \\ \int_0^L\int_0^L \rho C_p\dot{T}^h\varphi_i\varphi_j + \int_0^L\int_0^L \rho C_p u^h\cdot\nabla T\varphi_i - \int_0^L\int_0^L \frac{1}{RePr}(k\nabla T^h)\nabla\varphi - \\ \int_0^L\int_0^L \frac{1}{\gamma-1}\frac{dp^h}{dt}\phi + \sum_e\int_{\Omega^e} S(\varphi)\xi R2(T)d\Omega + \sum_e\int_{\Omega^e}\nabla\varphi\xi_{pspg}R2(T)d\Omega &= -\frac{1}{RePr}\left[k\nabla T^h\varphi\right]_0^L \end{aligned}$$

4.3 Adaptive Finite Element

Chapter 5

Bayesian Statistics

5.1 Review of Theory

In various sciences and engineering fields, uncertainity quantification problems arise. If we incorporate data into a model, significant reduction in uncertainty of model prediction is acheived and hence a very important step in many applicaiton. Bayes' formula provides the natural way to do this. Mathematical model governing physical phenomenon often include parameters that need to be determined from experiments by measuring them with the help of devices. The measures values of the parameters have uncertainty in them depending upon the assumptions, noise levels, models and prior knowledge. To estimate the correct values of the parameters we should make assumptions about the noise levels, models and prior knowledge. Let y be the data which is dependent on u.

$$y = G(u)$$

.
The solution of the inverse problem is the probability distribution of u given y, denoted by $u|y$. The Bayes' formula is given as

$$P(u|y) = \frac{P(u)P(y|u)}{P(y)}$$

.

Where $P(u)$ is the prior probability distribution of u. $P(y|u)$ is the likelihood of y given u. $P(y)$ is the scaling factor. In Bayesian approach, u is treated as random variable with some specified prior probability distribution that incorporates any prior knowledge about u that we believe is true and is independent of the measured data y. The result is the posterior probability distribution of u conditional on y. The likelihood and prior are selected as per (.....) .

5.2 Application to Problem

5.3 Methods of Solution

5.4 Software

Chapter 6

Results

6.1 Estimating parameter E for reaction 3

The results displayed in this section are for the uncertainty involved in the calculation of flamespeed depending ony on one parameter i.e the activation energy for the fall off reaction in the ozone mechanism. The results are dispalyed in two section. In first section, The sample size for surrogate is changed and it is clear that for varying sized the map point of the resulting pdf does not change greatly. The surrogate are constructed using linear interpolation function. The initial guess for the map point is calculated using nelder mead optimization technique. After supplying initial guess over large domain it is found that the map point is the same no matter where we start our guess.

Different surrogate sizes

Here the surrogate size is defined as $samplesize * 1$ vector. The flamespeed is calculated for given samples in the domain (0 to 34.76). Other values are calculated as linear interpolation of these points. In this analysis, constant raw chain size of 500,000 is taken.

Sample size (Surrogate size) 10

In this section we calculated flamespeed values for 10 different points in the domain and the remaining values are linear combination of these 10 points.

Sample size (Surrogate size) 20

In this section we calculated flamespeed values for 20 different points in the domain and the remaining values are linear combination of these 20. We can see that our results do not change drastically.

Sample size (Surrogate size) 50

In this section we calculated flamespeed values for 50 points in the domain

Sample size (Surrogate size) 100

In this section we calculated flamespeed values for 100 points in the domain

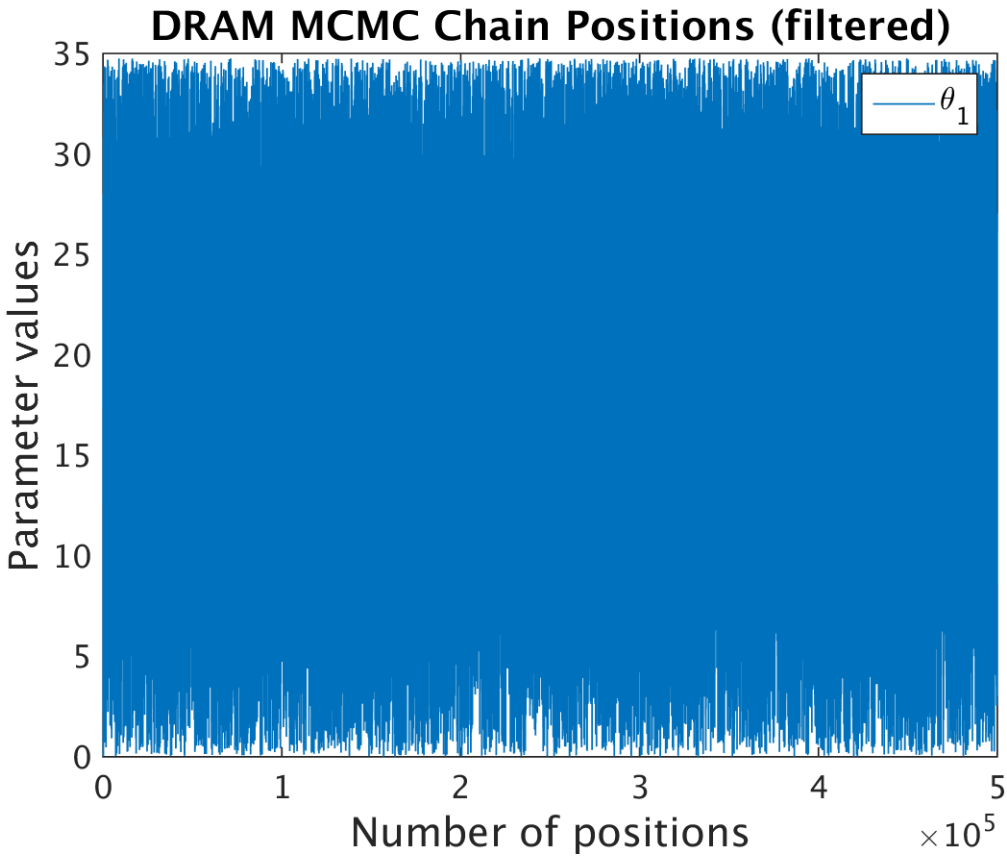

Figure 6.1: MCMC chain position

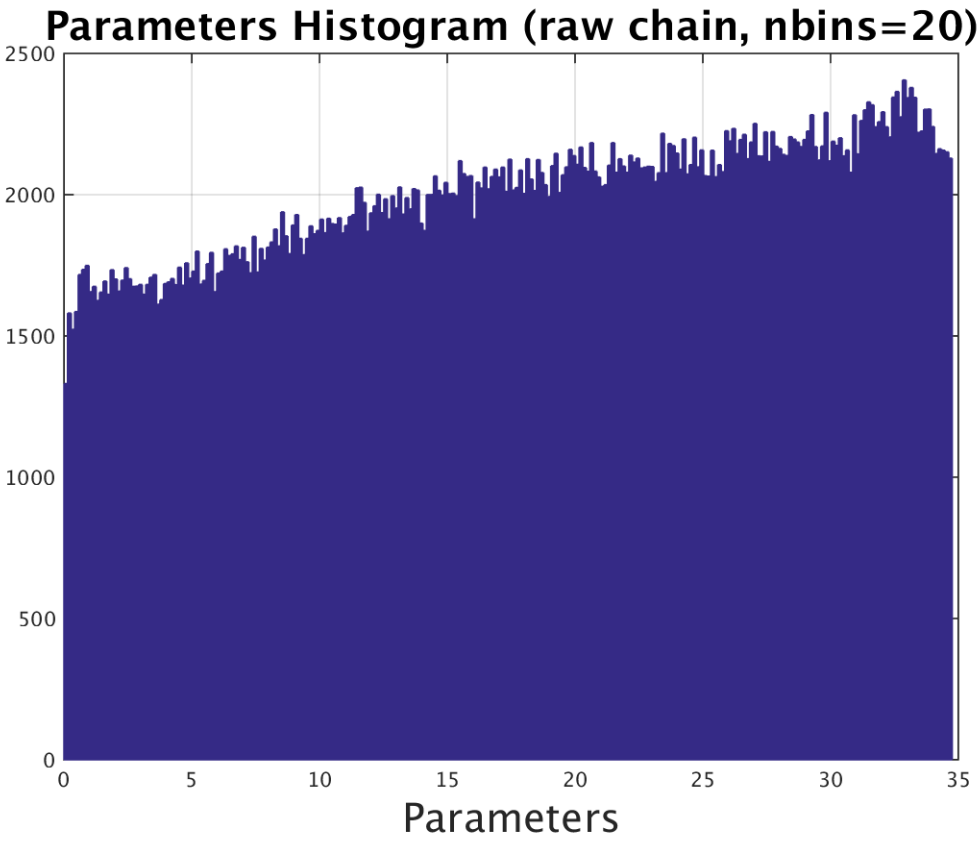

Figure 6.2: Histogram

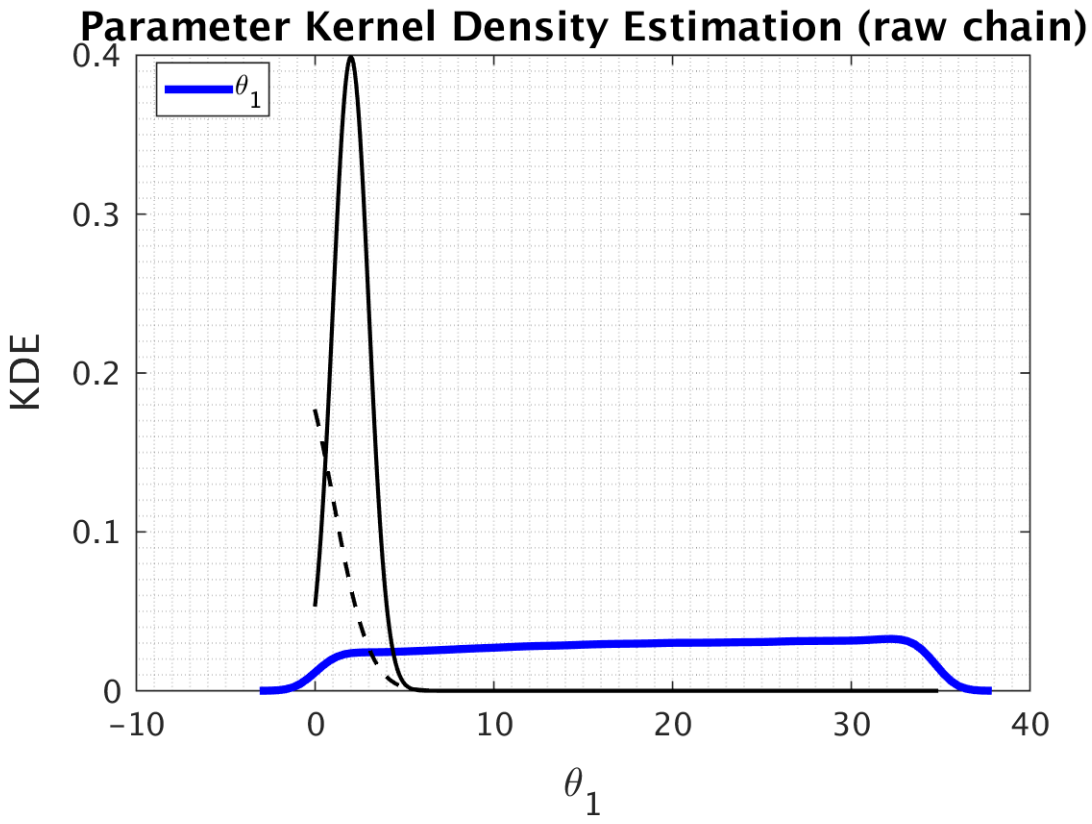

Figure 6.3: KDE

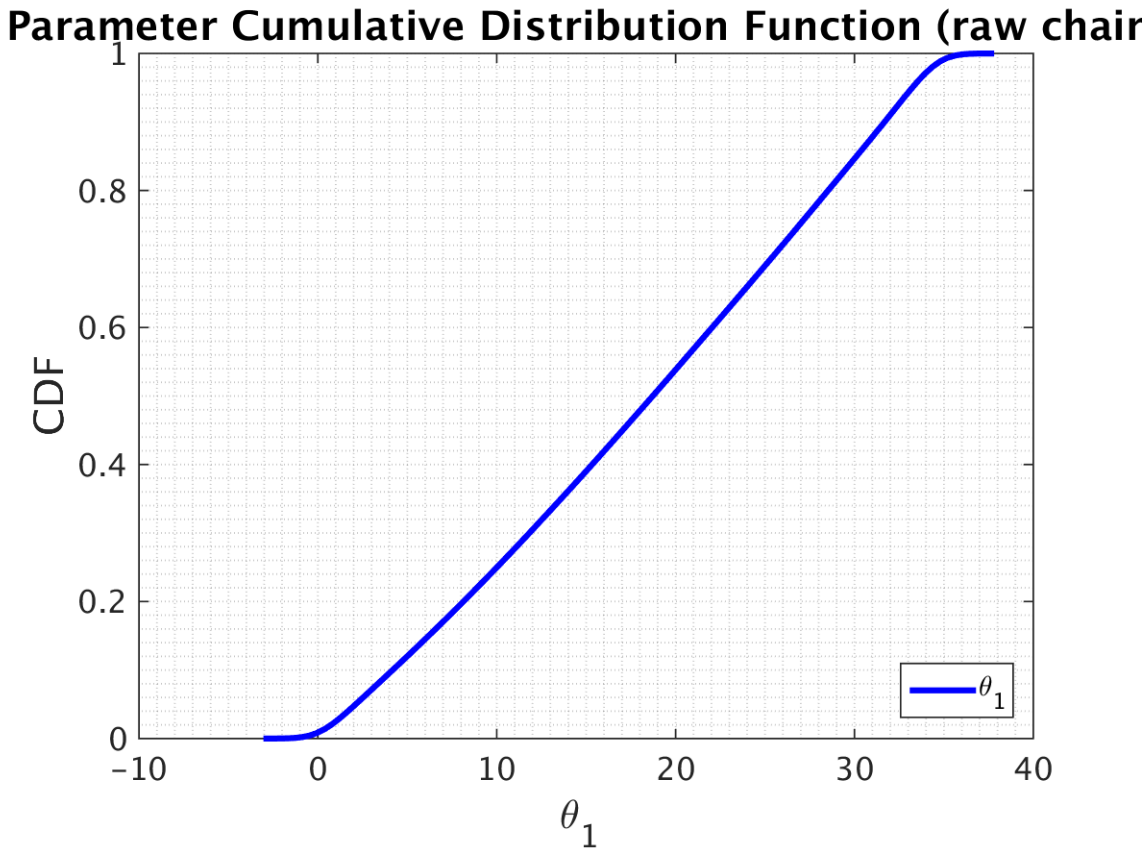

Figure 6.4: CDF function for Parameter

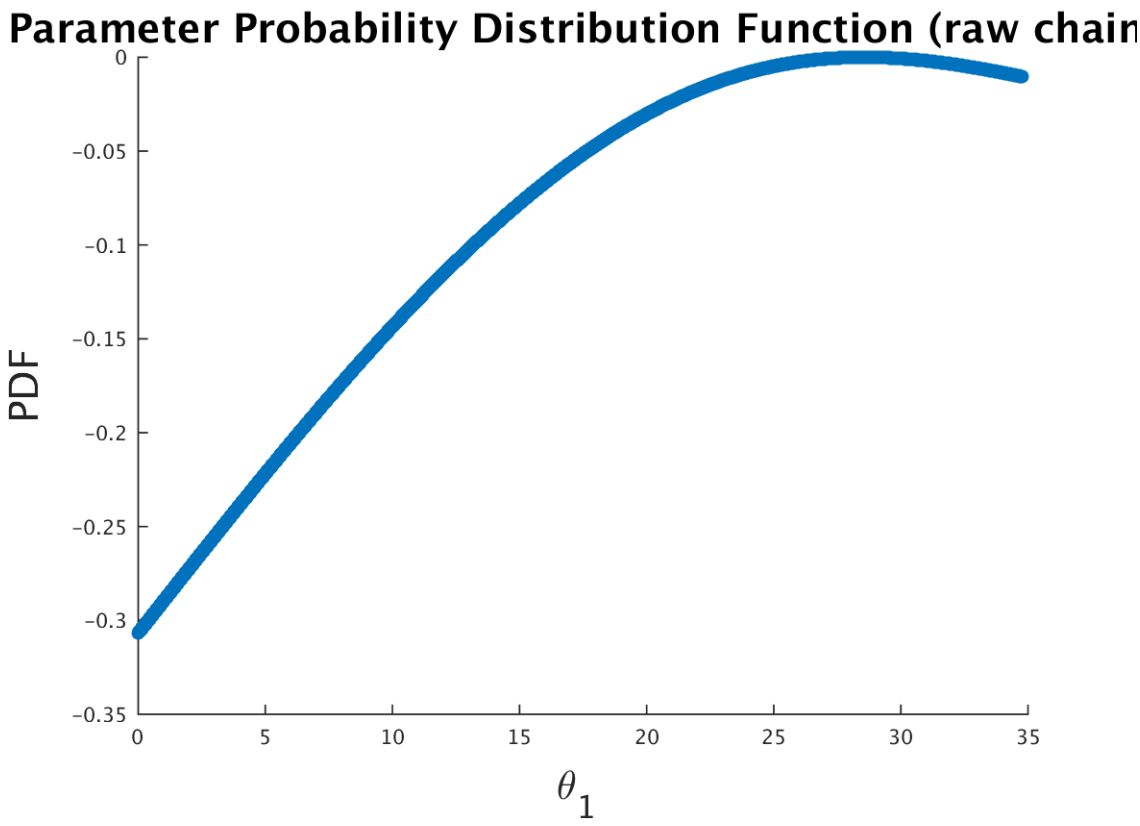

Figure 6.5: PDF function for Parameter

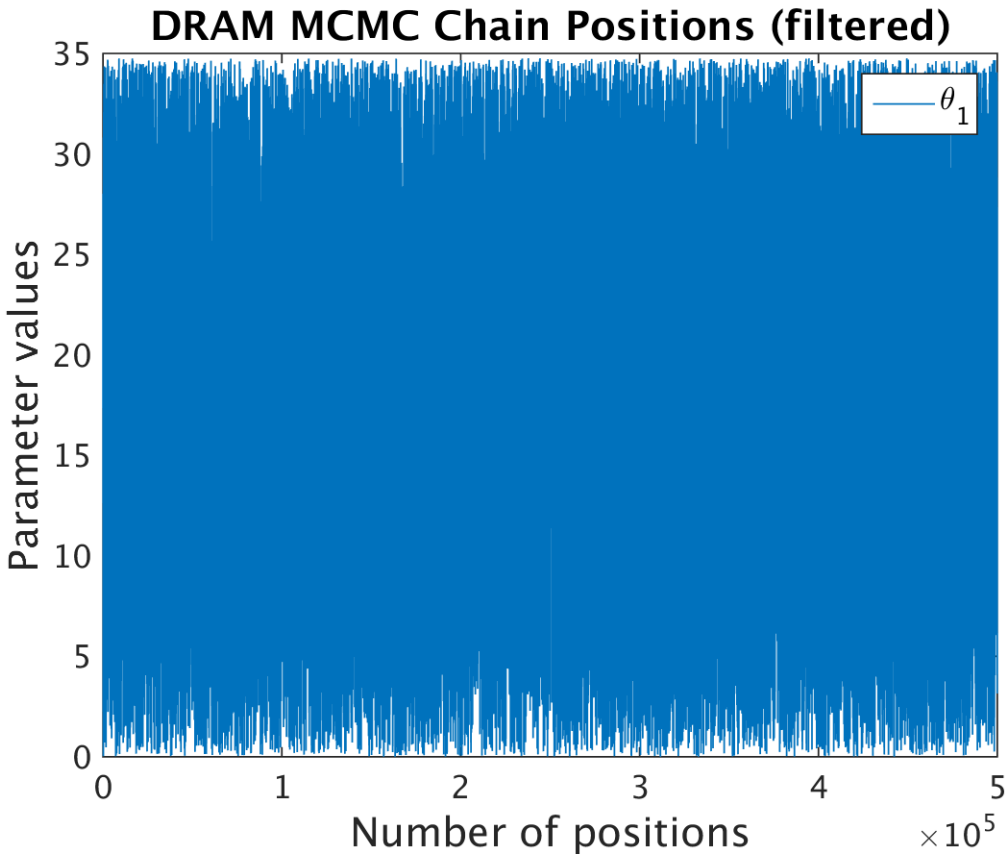

Figure 6.6: MCMC chain position

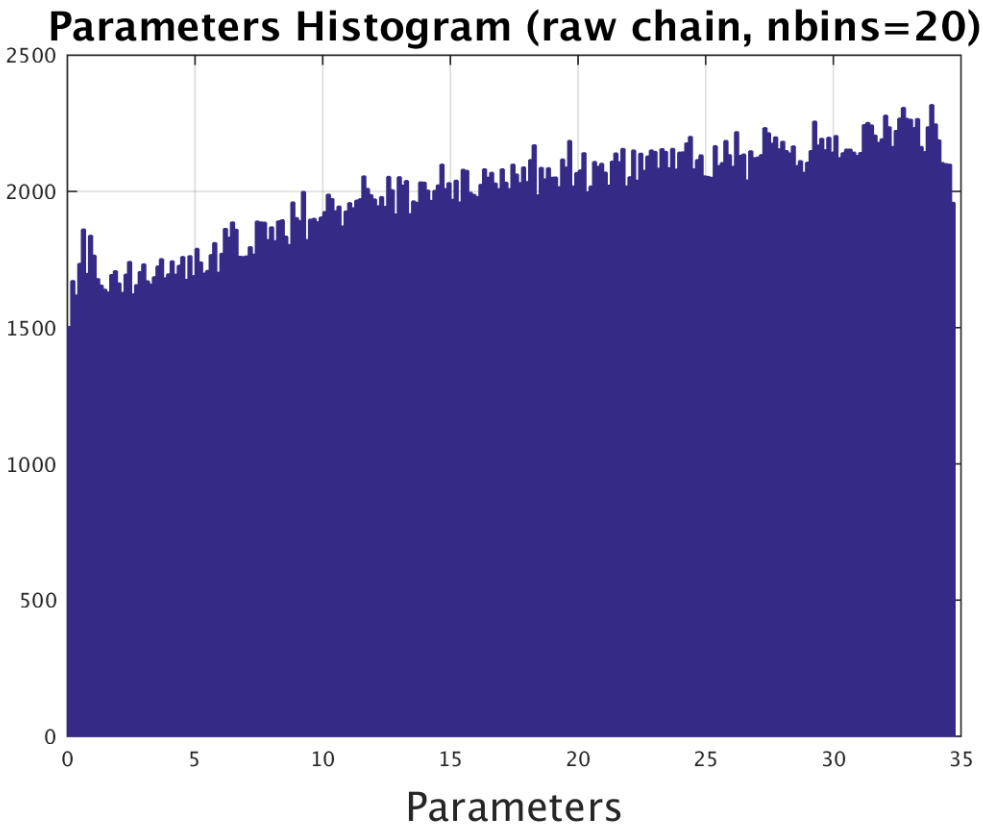

Figure 6.7: Histogram

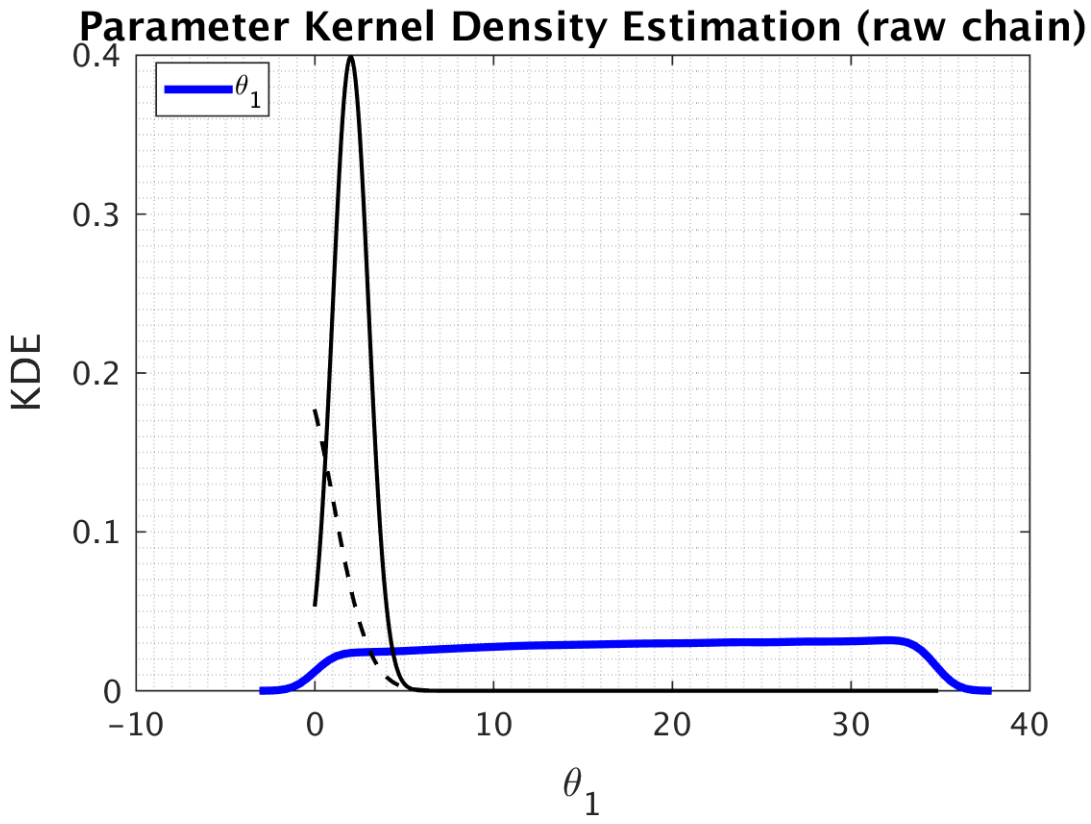

Figure 6.8: KDE

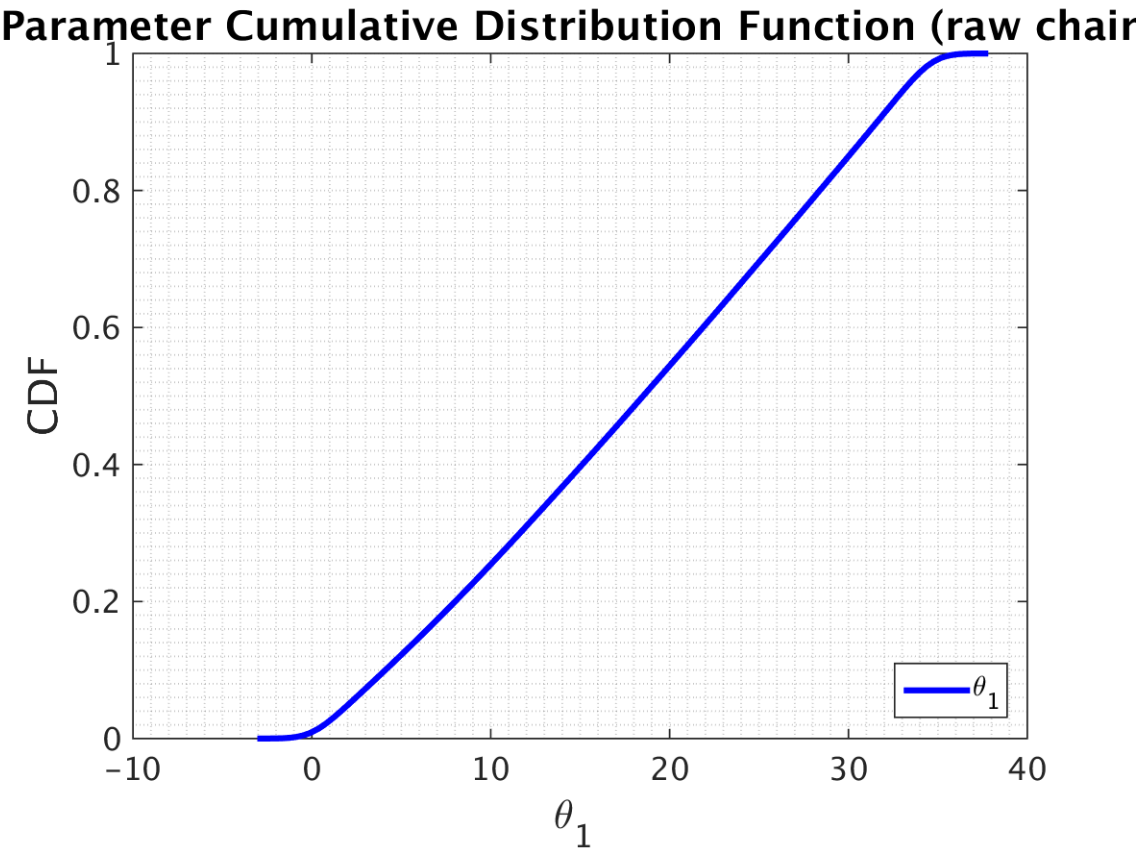

Figure 6.9: CDF function for Parameter

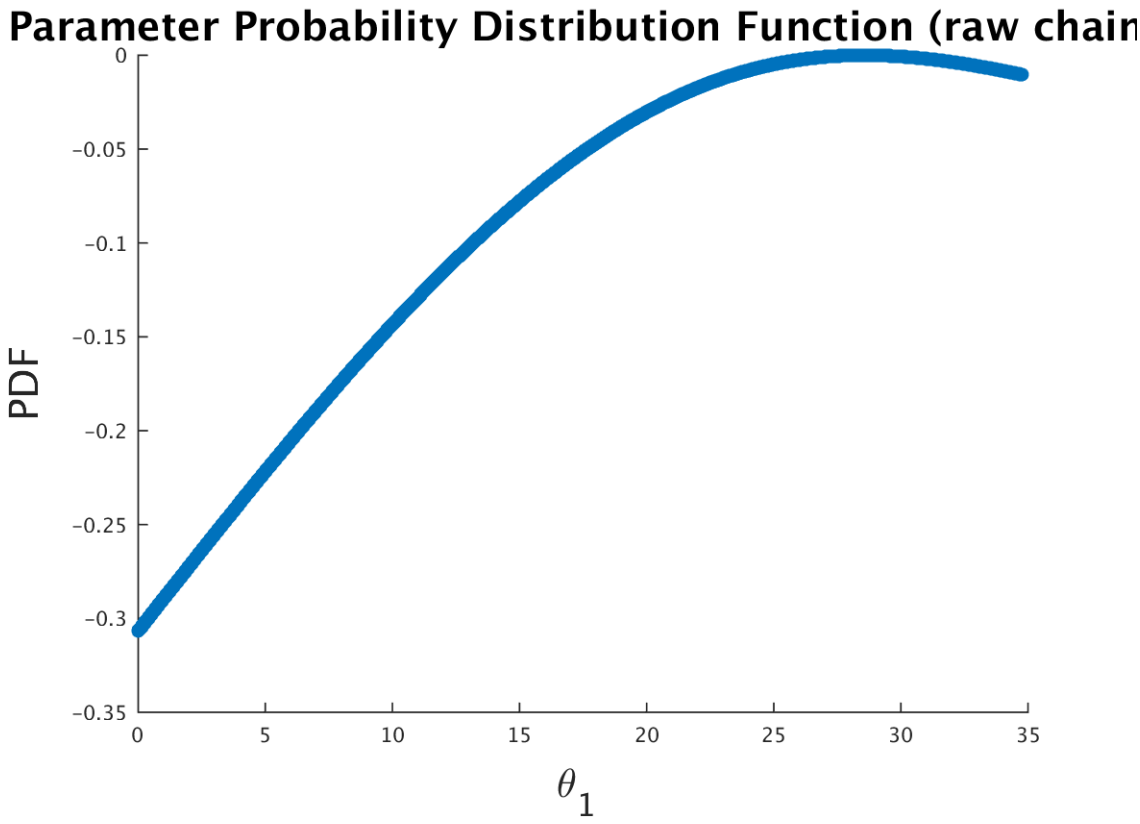

Figure 6.10: PDF function for Parameter

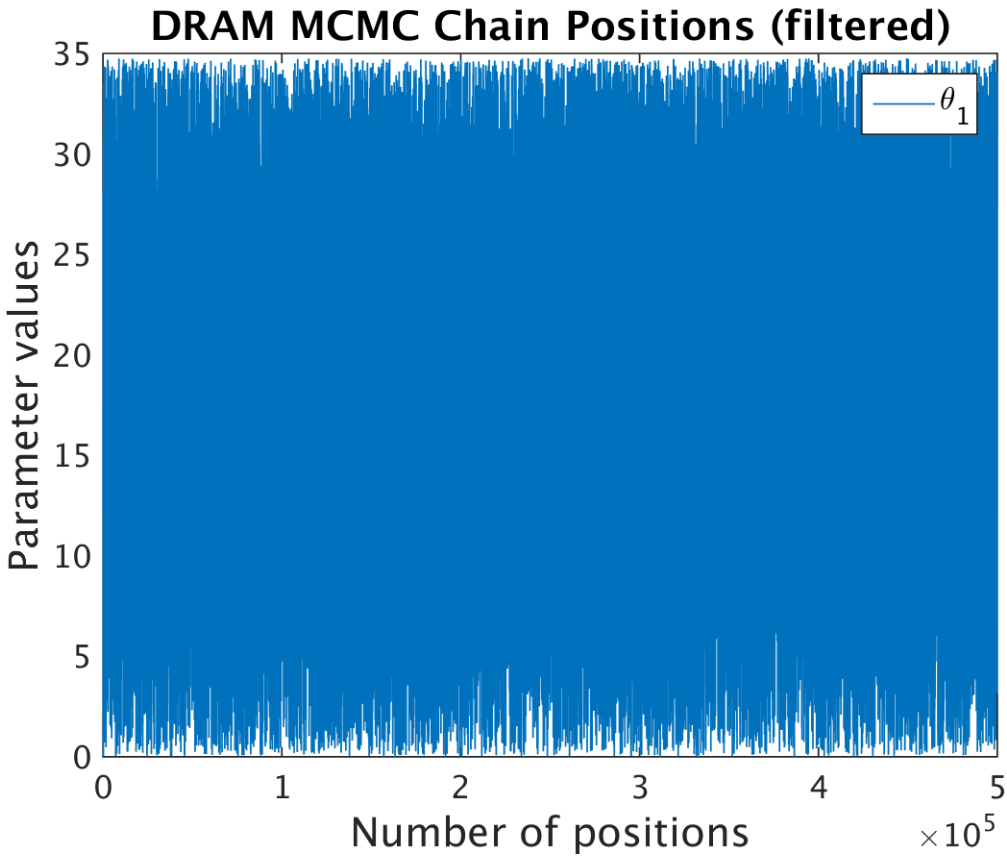

Figure 6.11: MCMC chain position

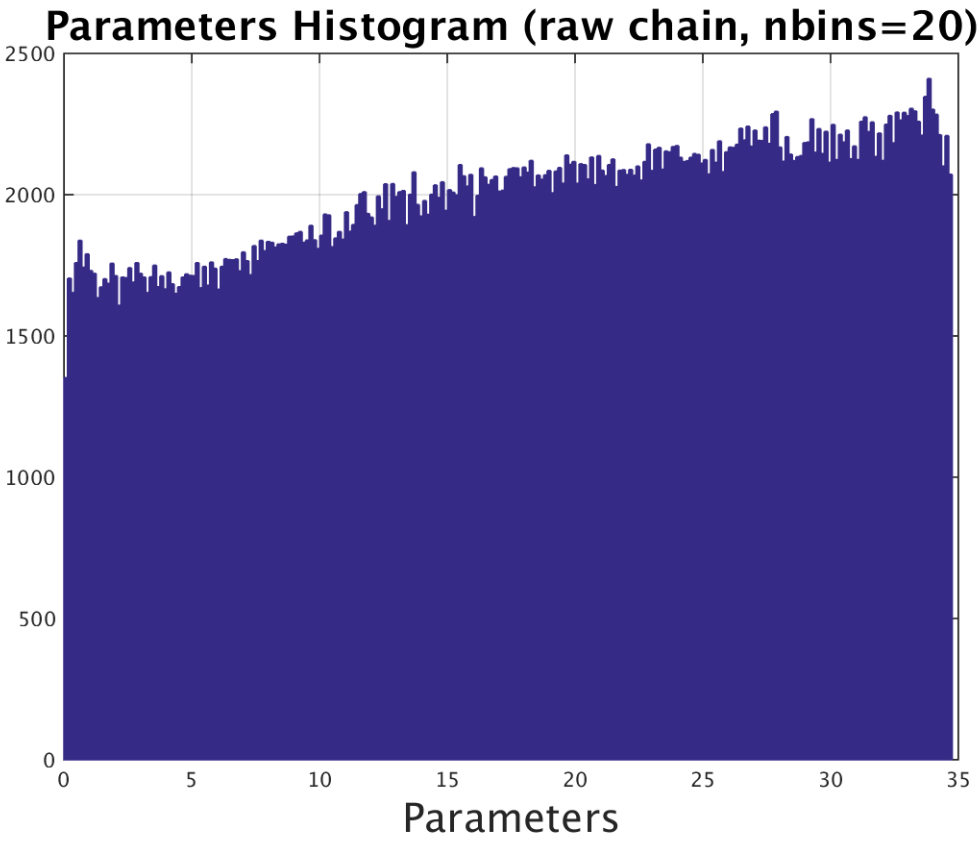

Figure 6.12: Histogram

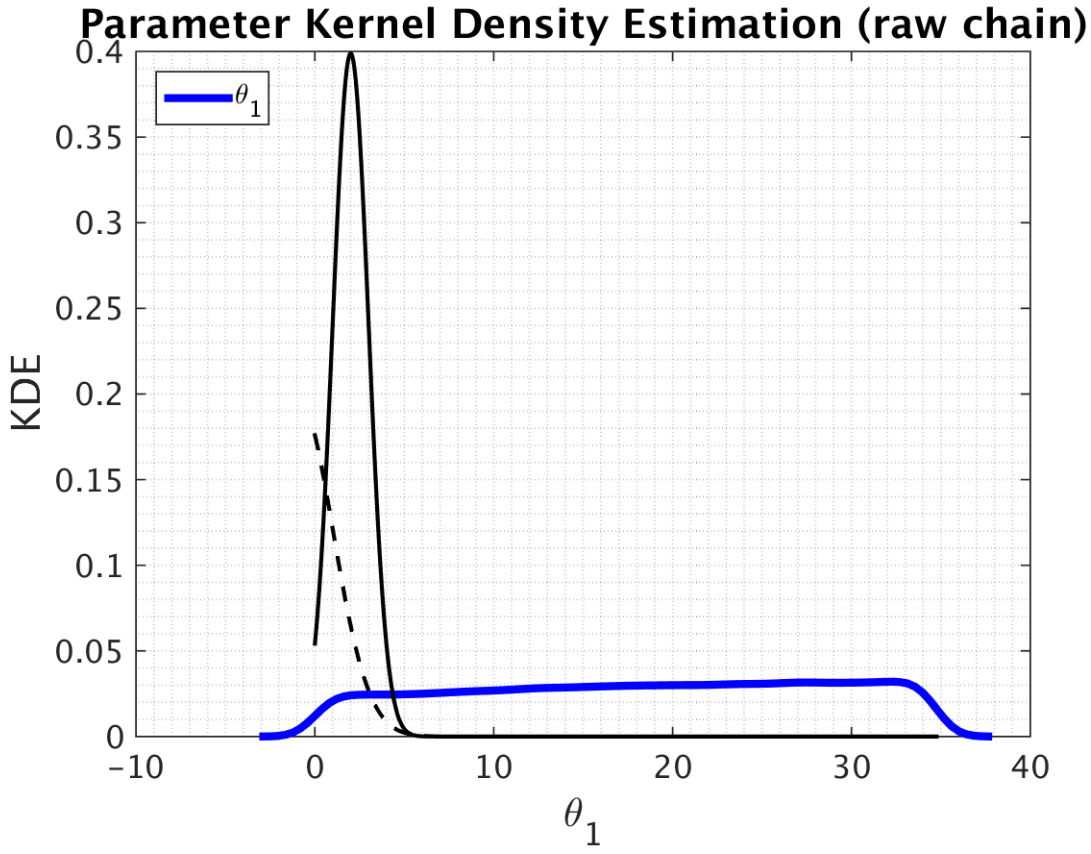

Figure 6.13: KDE

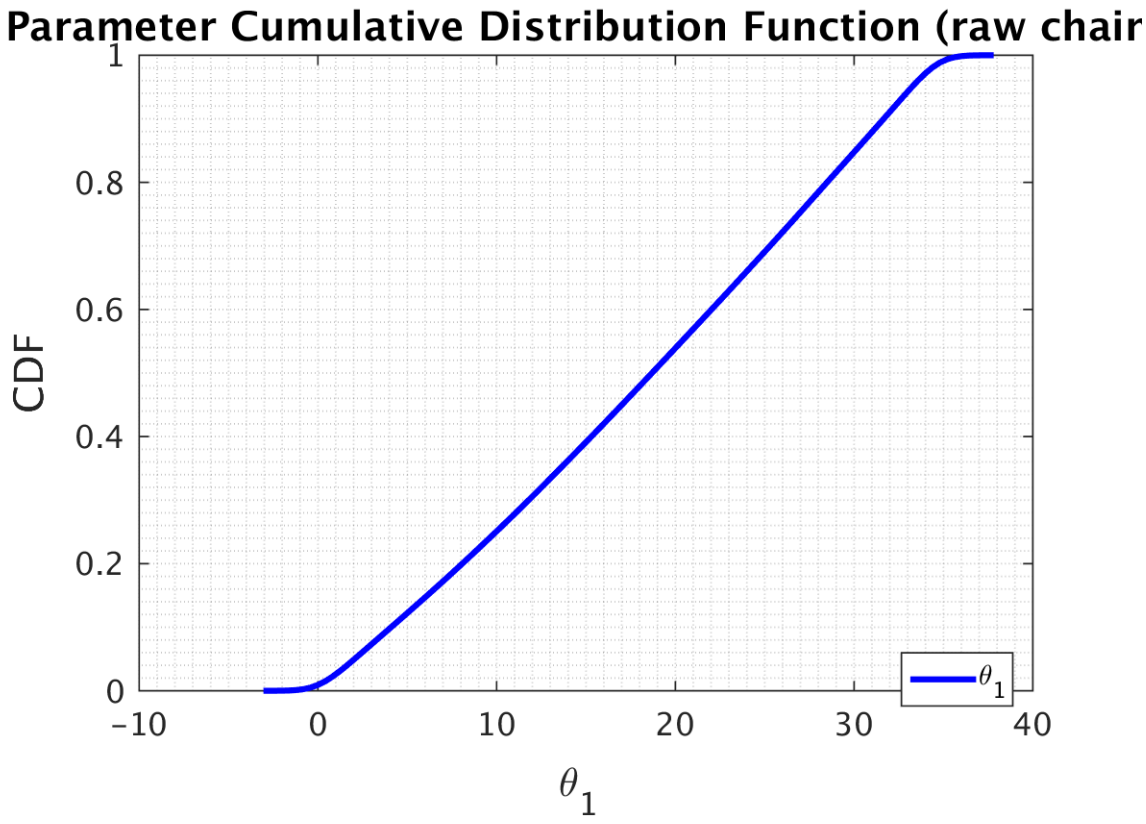

Figure 6.14: CDF function for Parameter

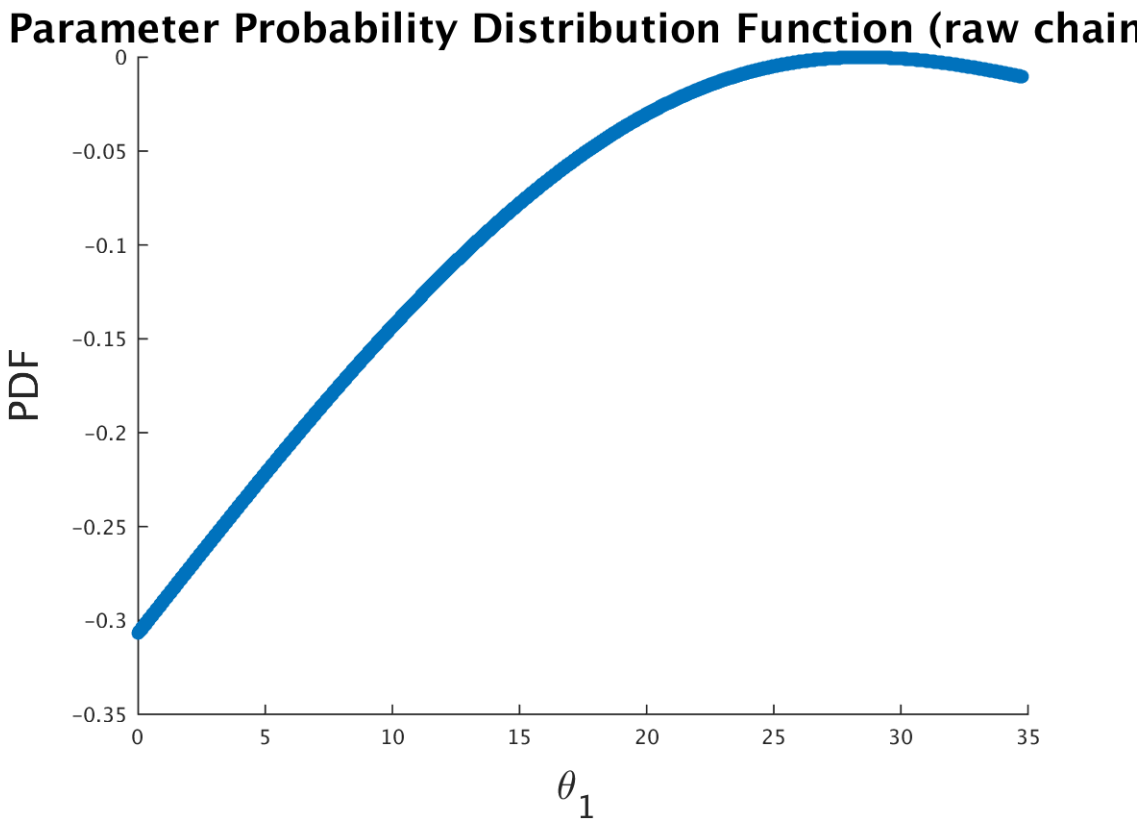

Figure 6.15: PDF function for Parameter

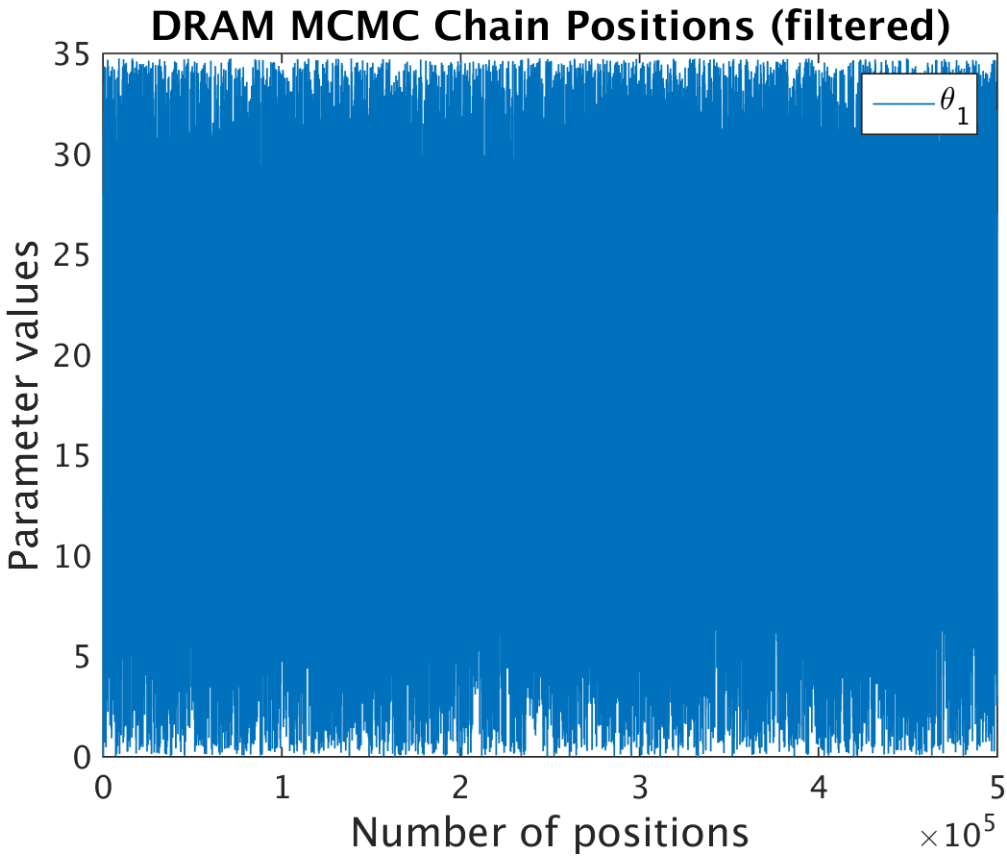

Figure 6.16: MCMC chain position

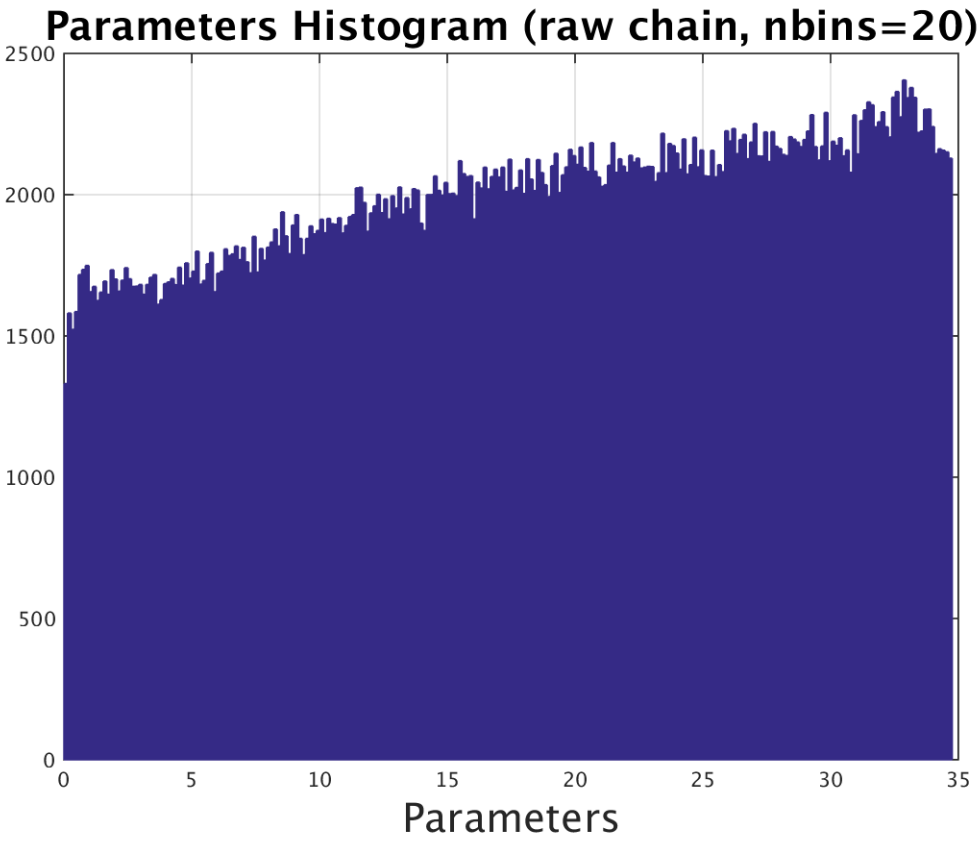

Figure 6.17: Histogram

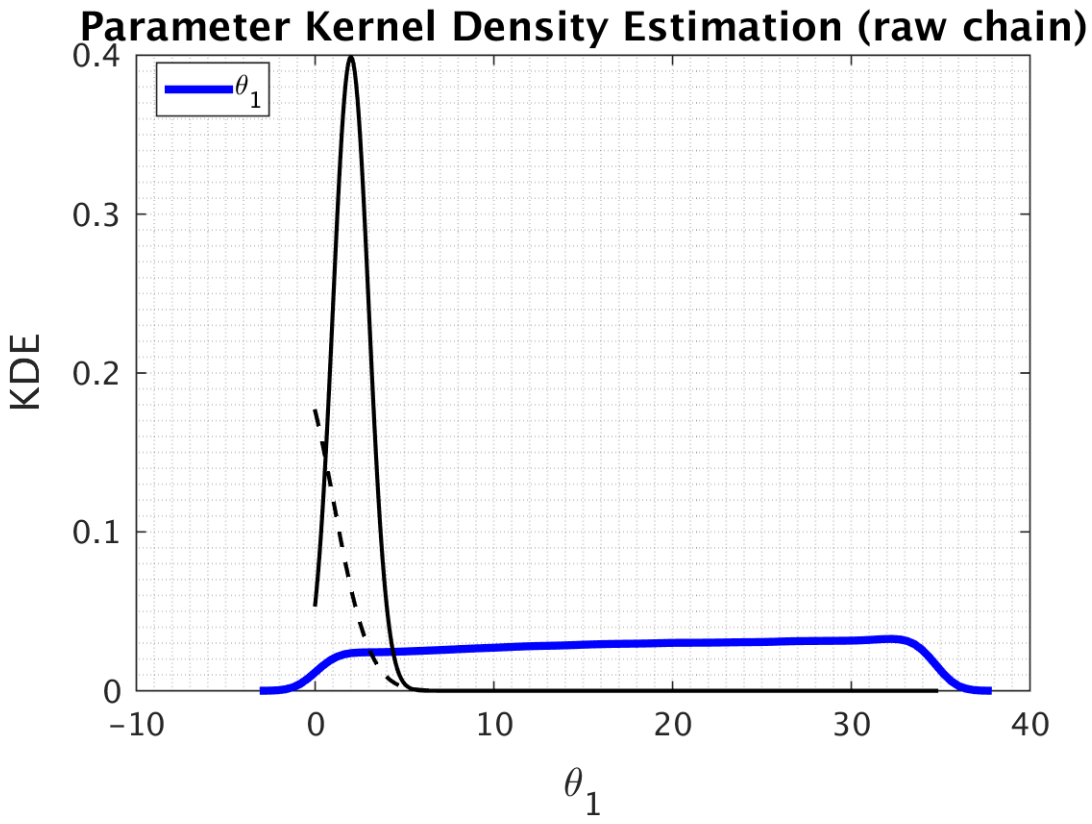

Figure 6.18: KDE

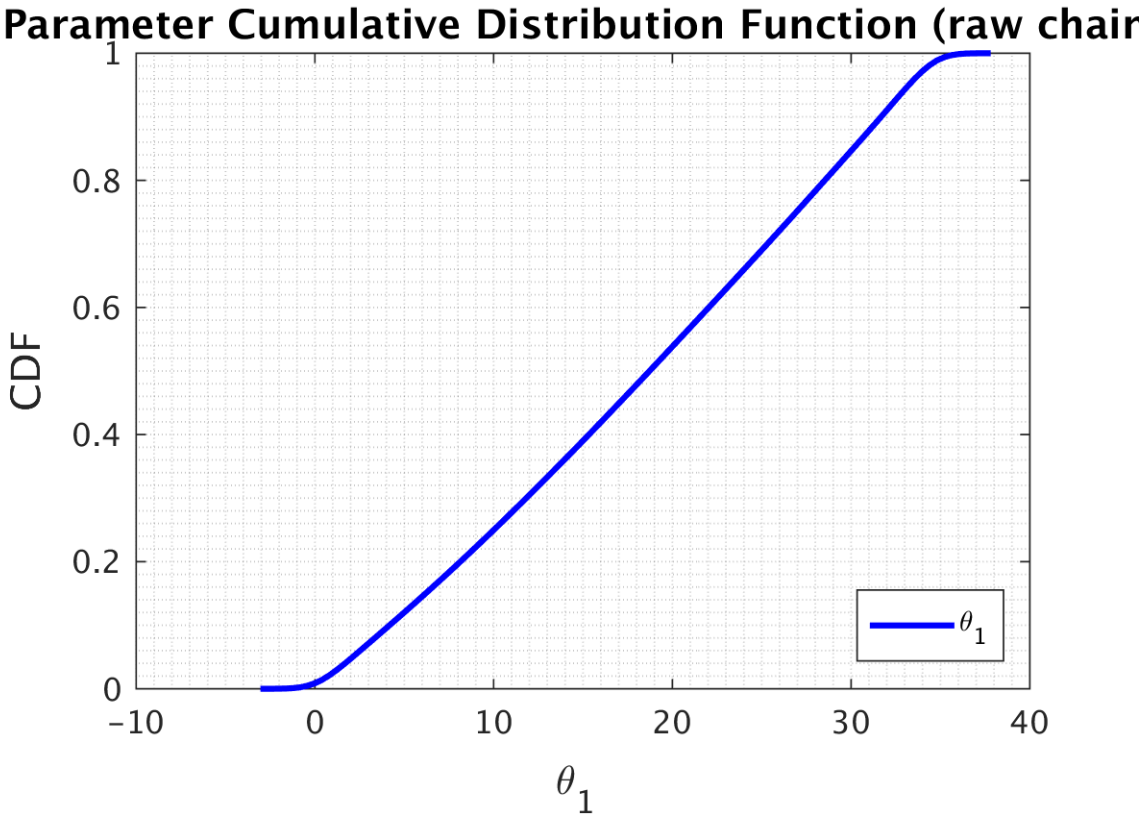

Figure 6.19: CDF function for Parameter

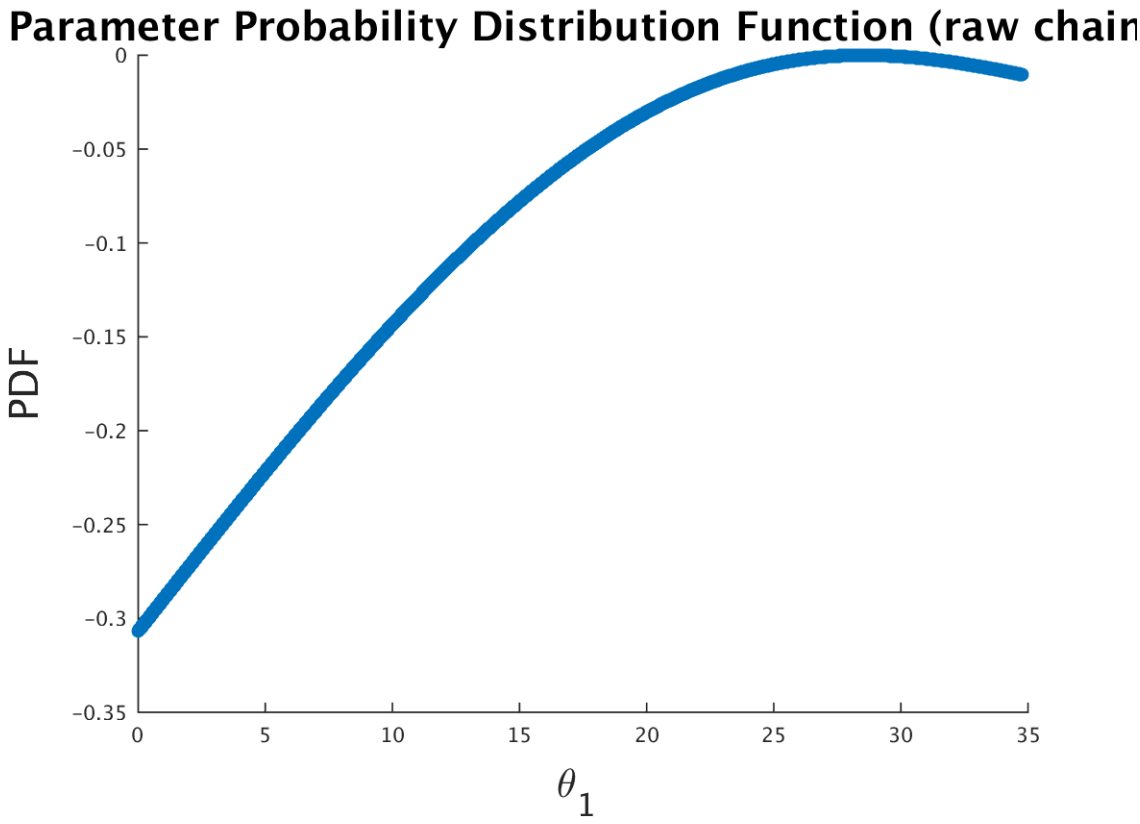

Figure 6.20: CDF function for Parameter

Sample size (Surrogate size) 500

In this section we calculated flamespeed values for 500 points in the domain

Sample size (Surrogate size) 1000

In this section we calculated flamespeed values for 1000 points in the domain

Different chain sizes

In this section we calculated flamespeed values for 100 different points in the domain and the remaining values are linear combination of these 100. we change the size of raw chain (mcmc chain size).

Chain size 100000

In this section we have chain size of 100000 points.

Chain size 300000

In this section we have chain size of 300000 points.

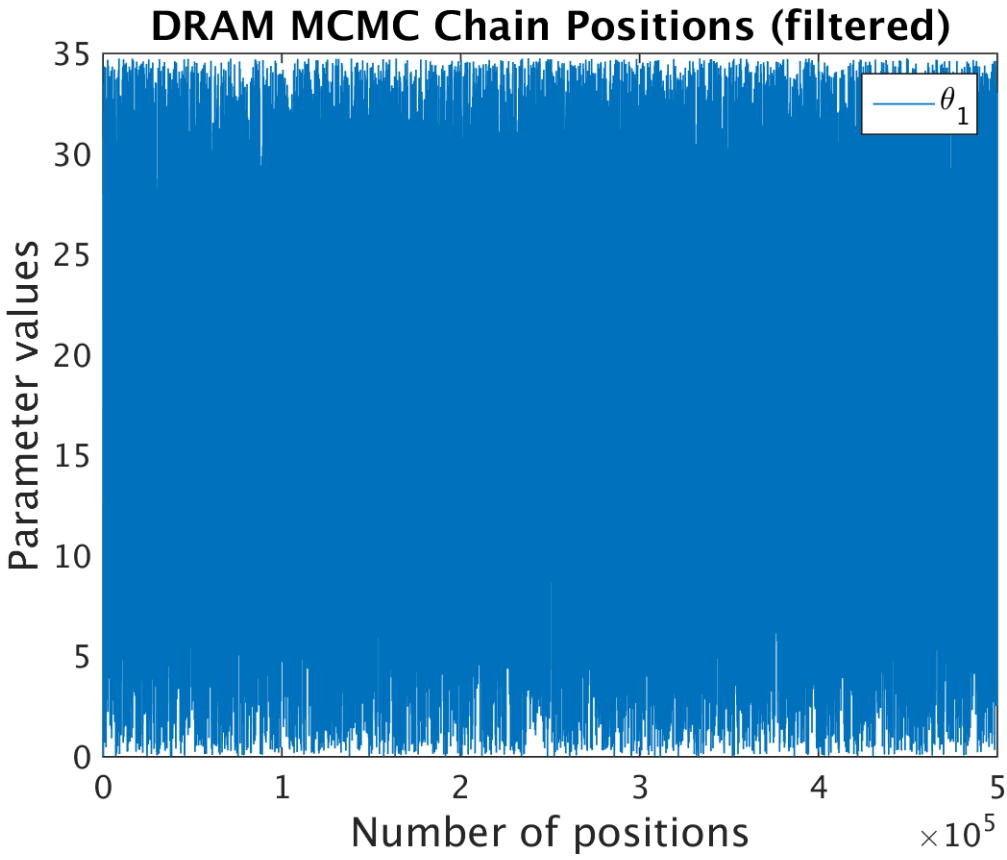

Figure 6.21: MCMC chain position

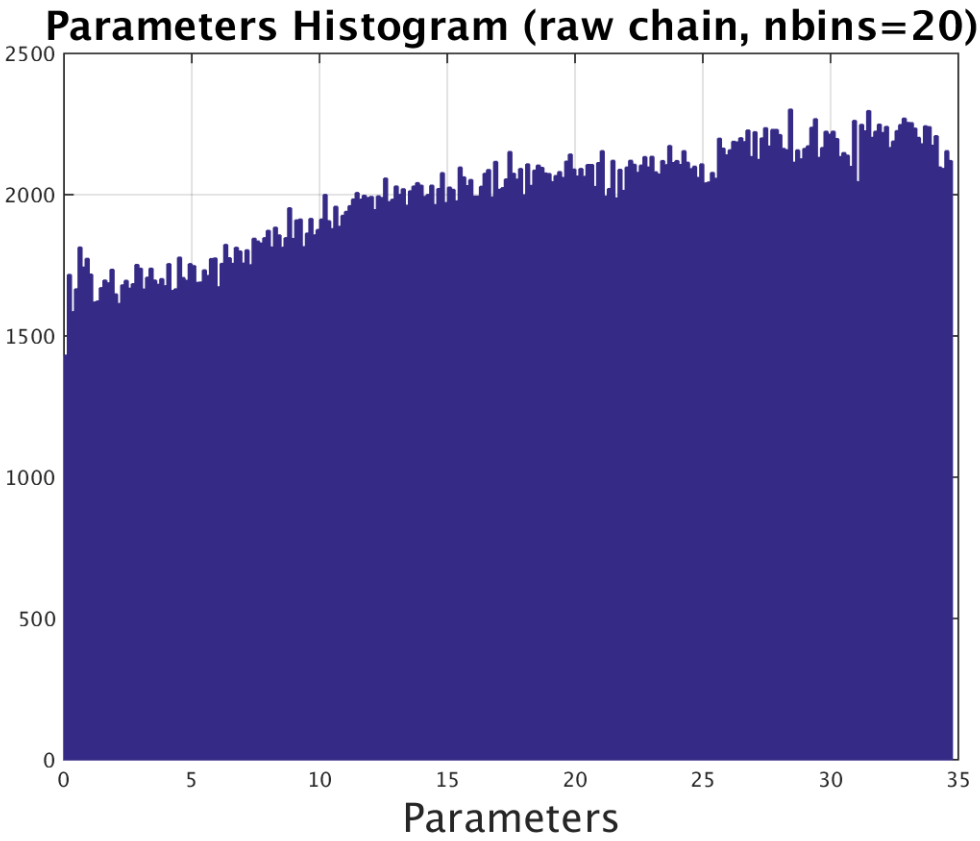

Figure 6.22: Histogram

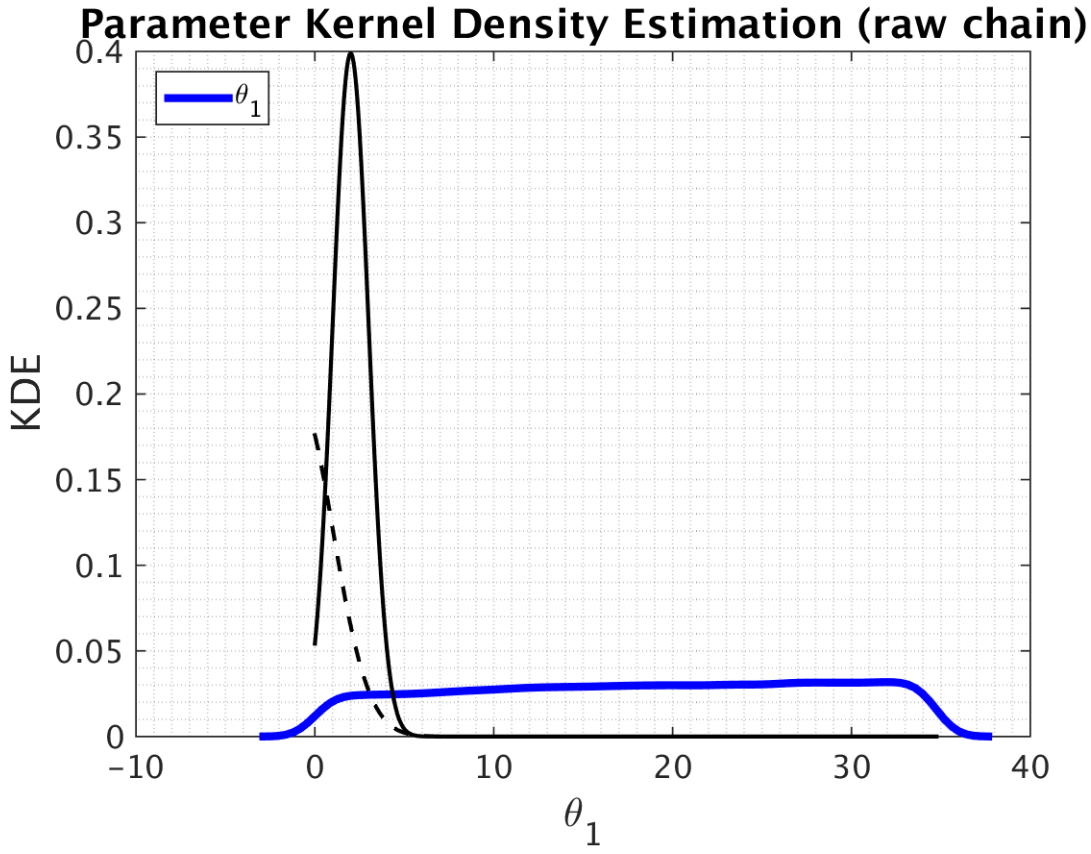

Figure 6.23: KDE

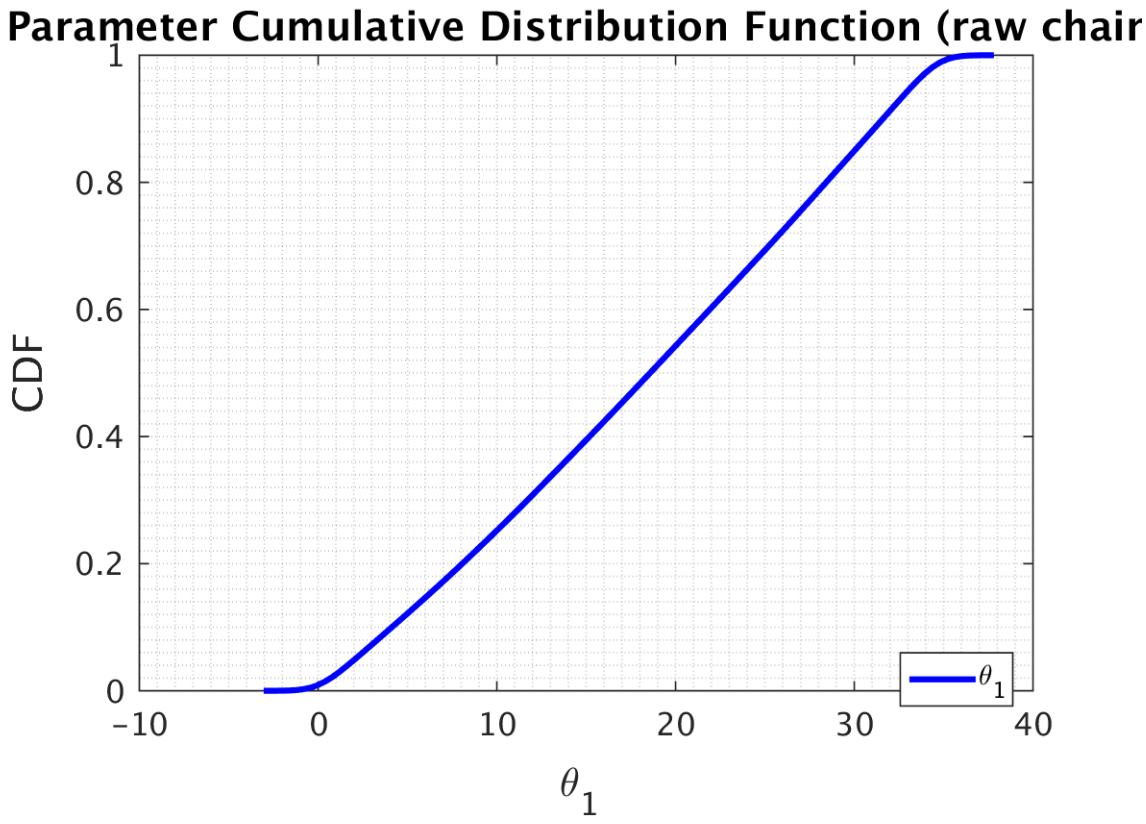

Figure 6.24: CDF function for Parameter

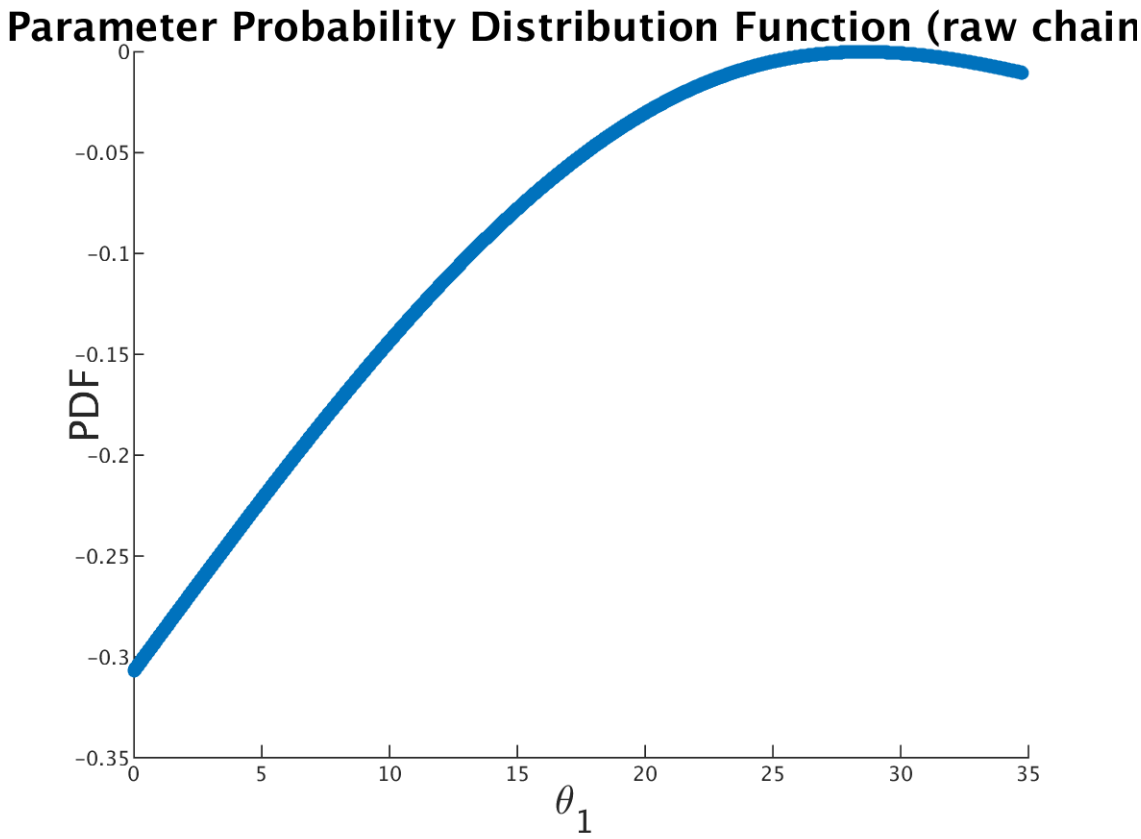

Figure 6.25: PDF function for Parameter

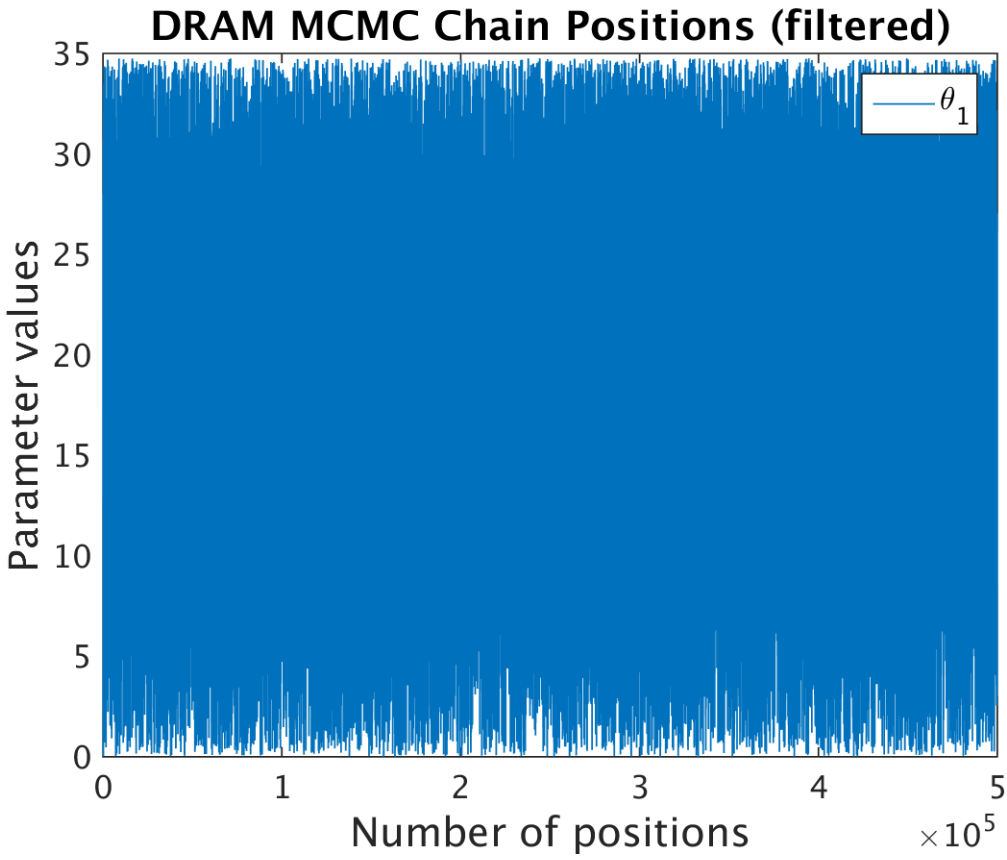

Figure 6.26: MCMC chain position

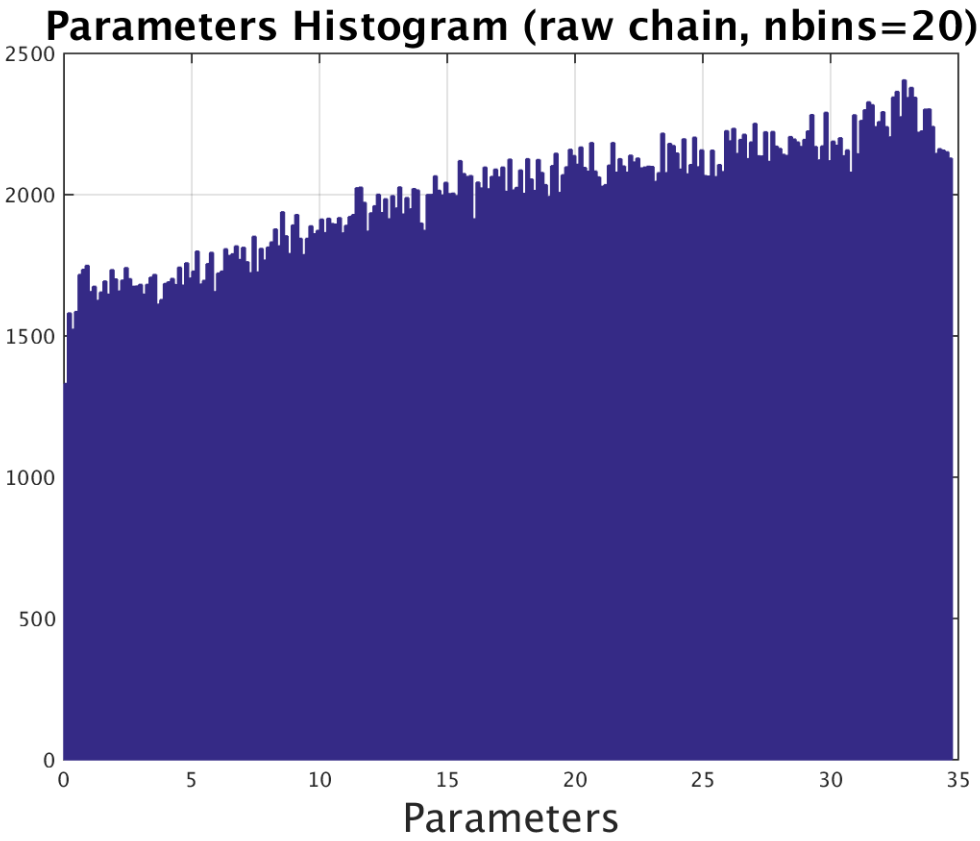

Figure 6.27: Histogram

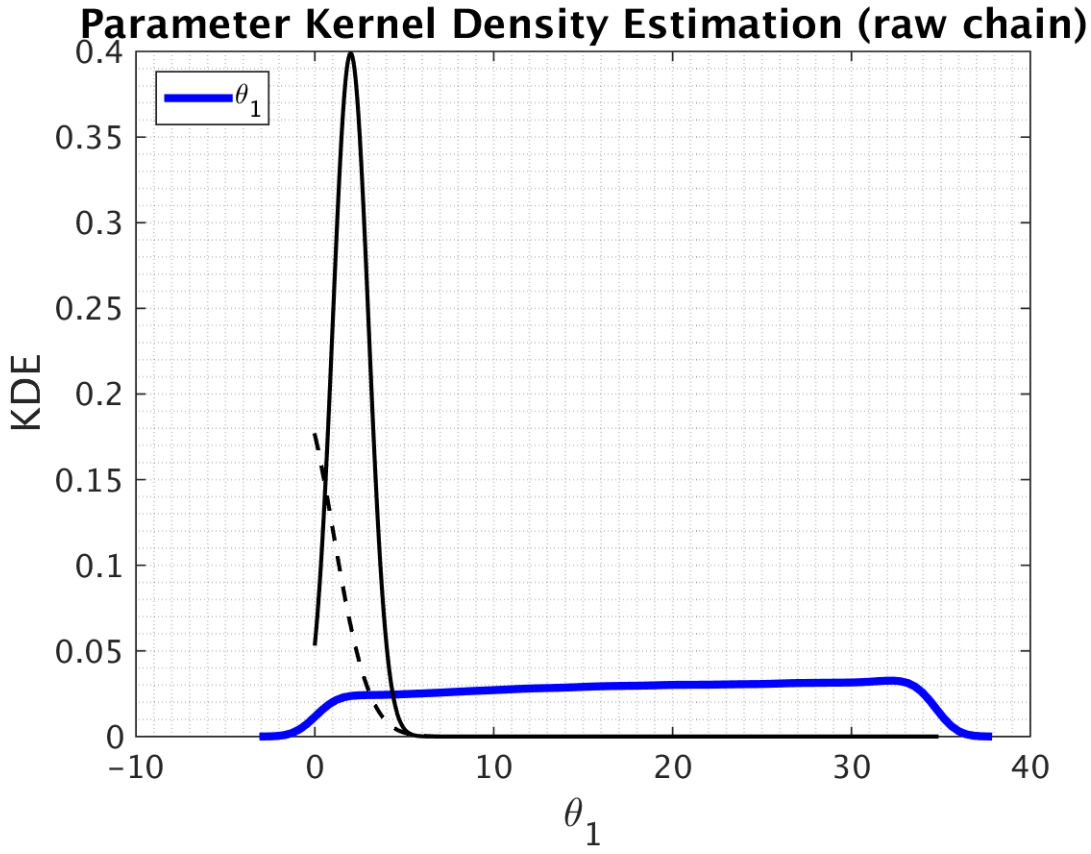

Figure 6.28: KDE

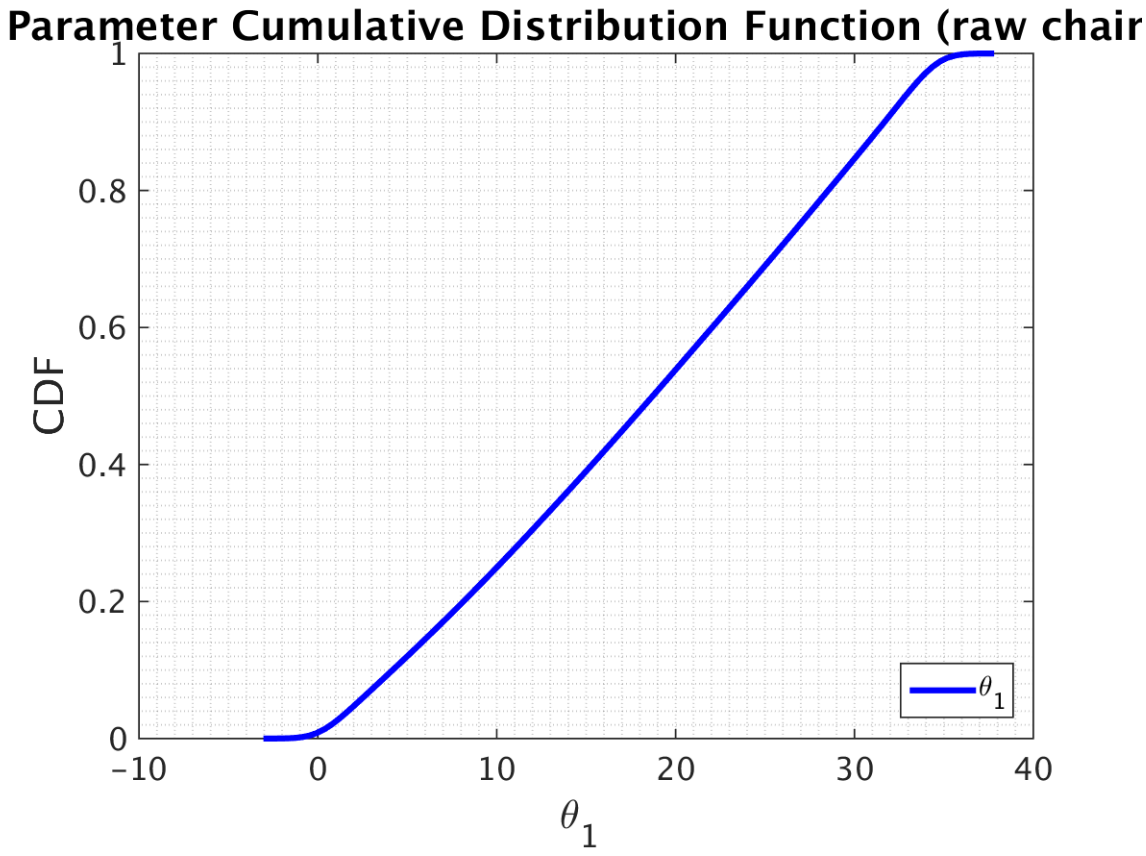

Figure 6.29: CDF function for Parameter

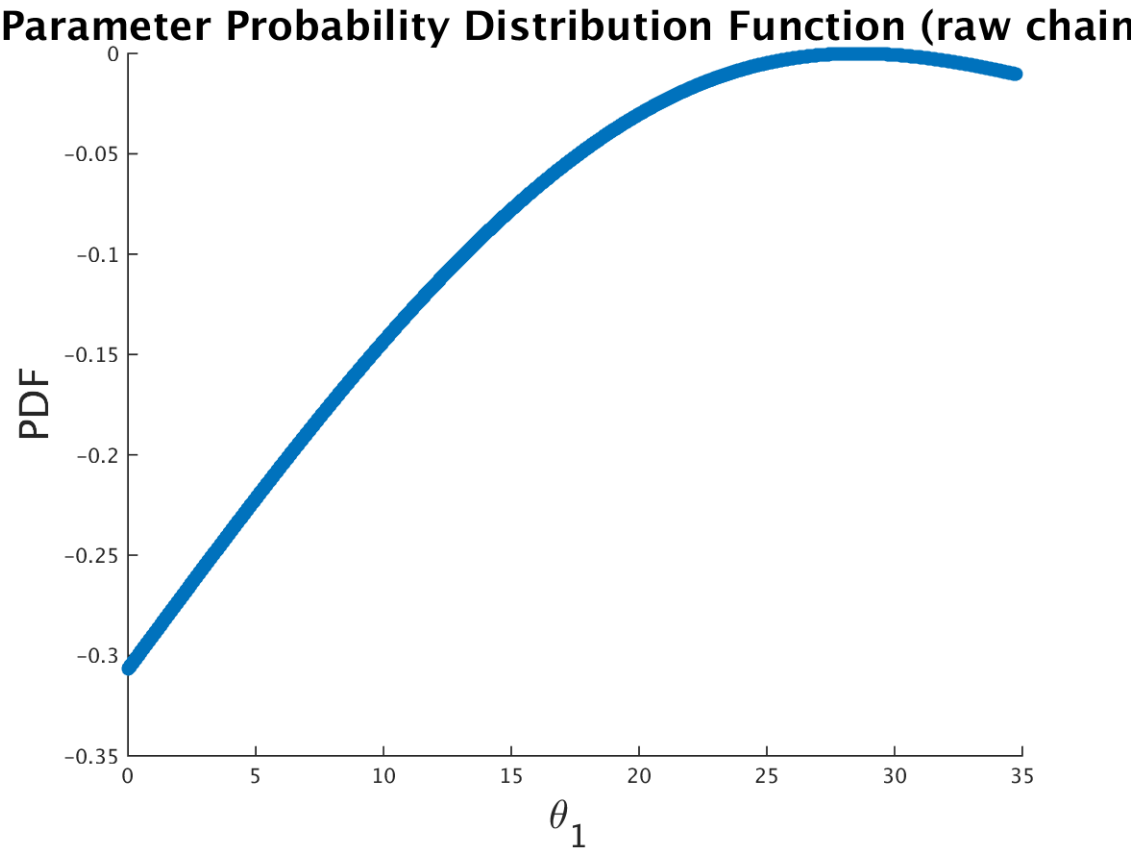

Figure 6.30: PDF function for Parameter

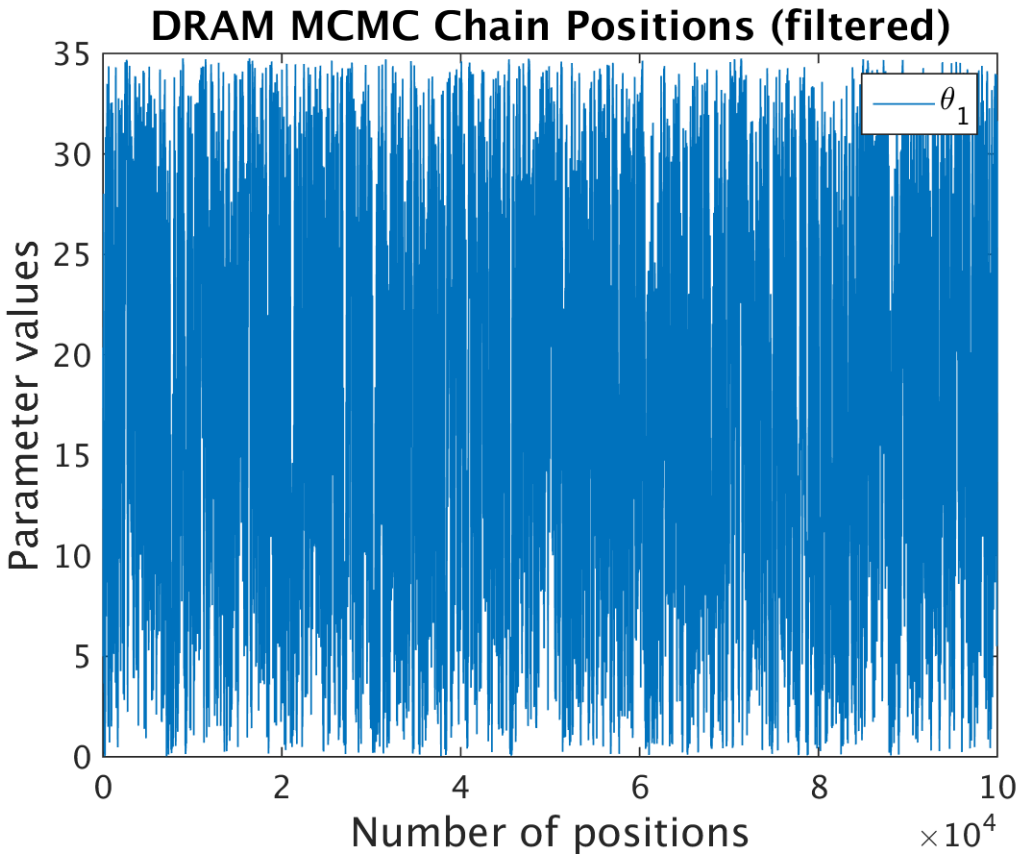

Figure 6.31: MCMC chain position

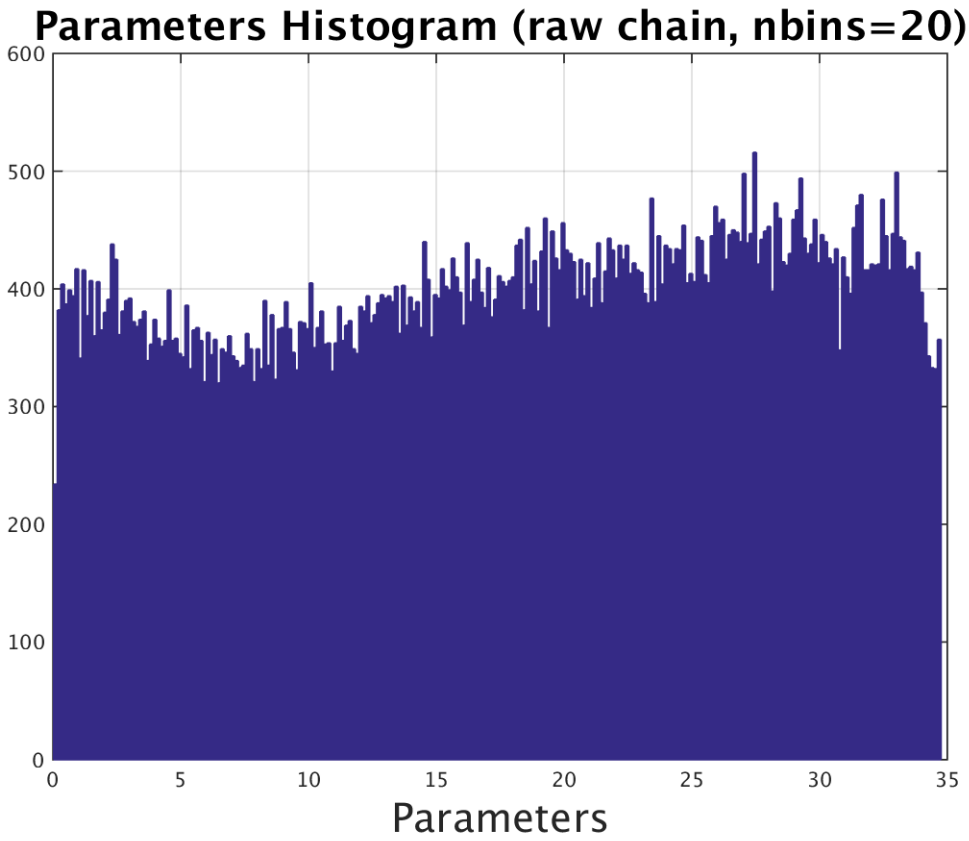

Figure 6.32: Histogram

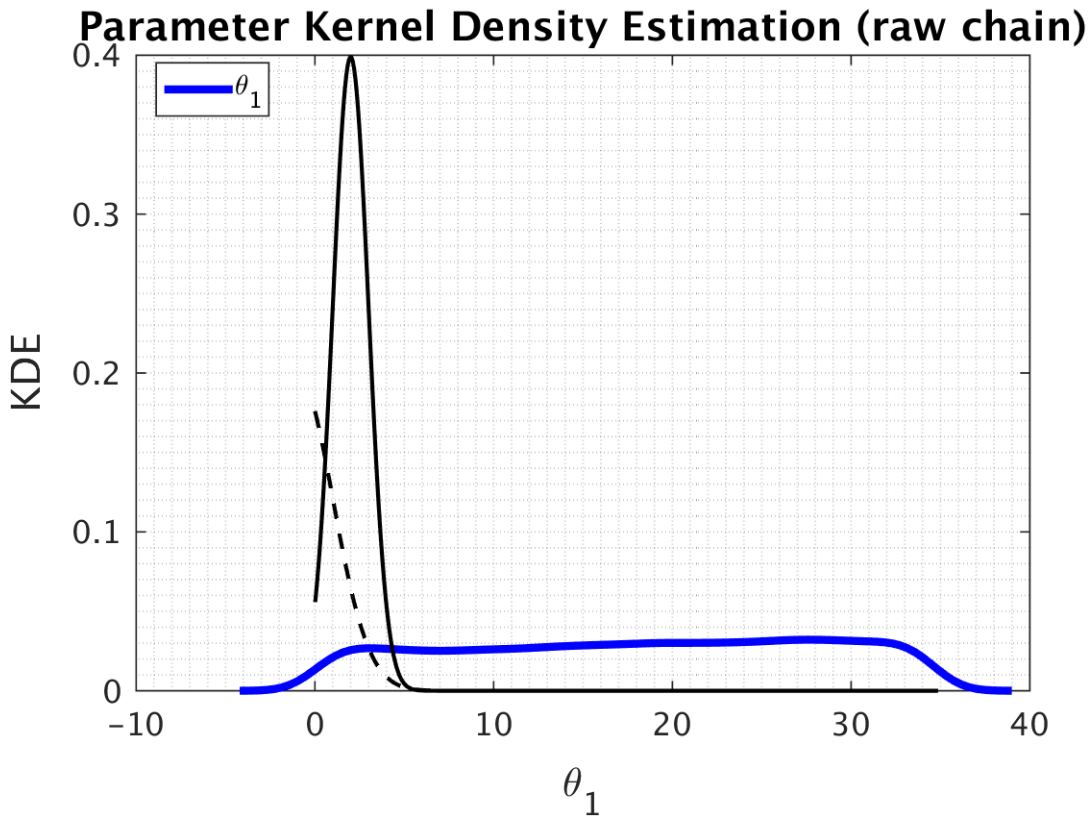

Figure 6.33: KDE

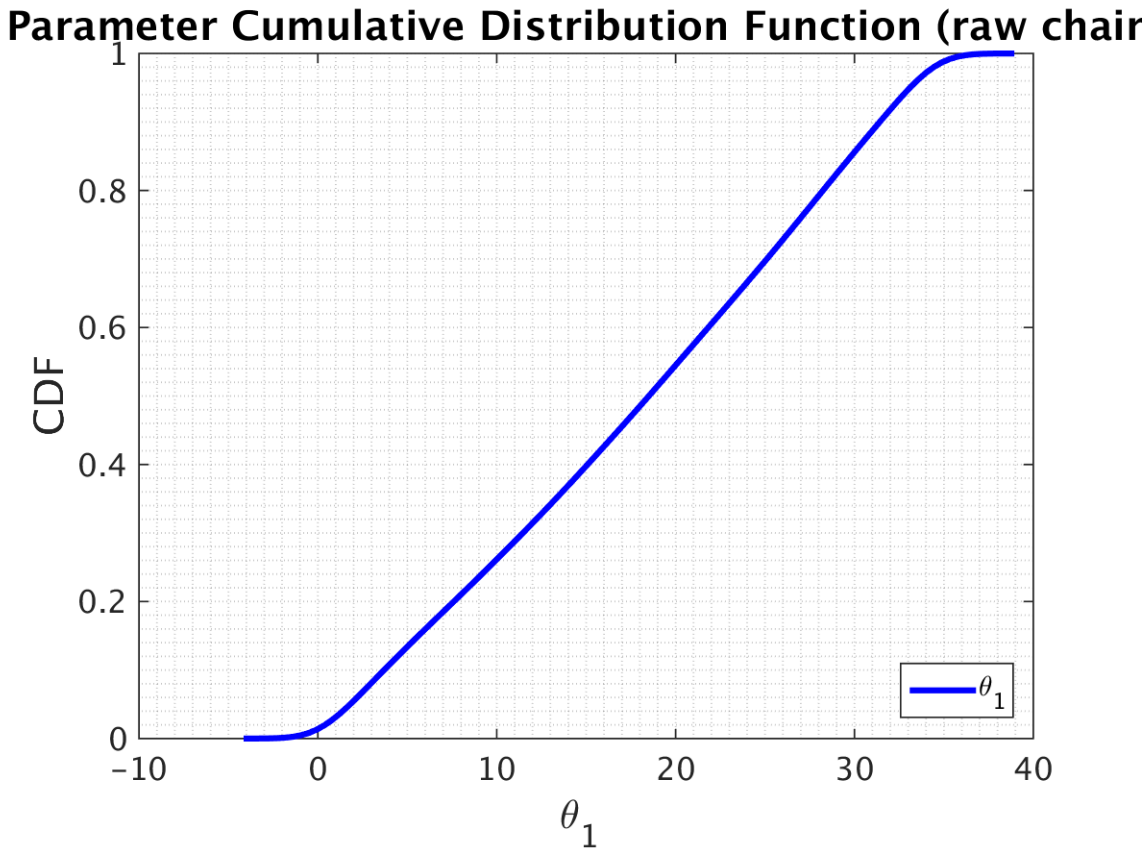

Figure 6.34: CDF function for Parameter

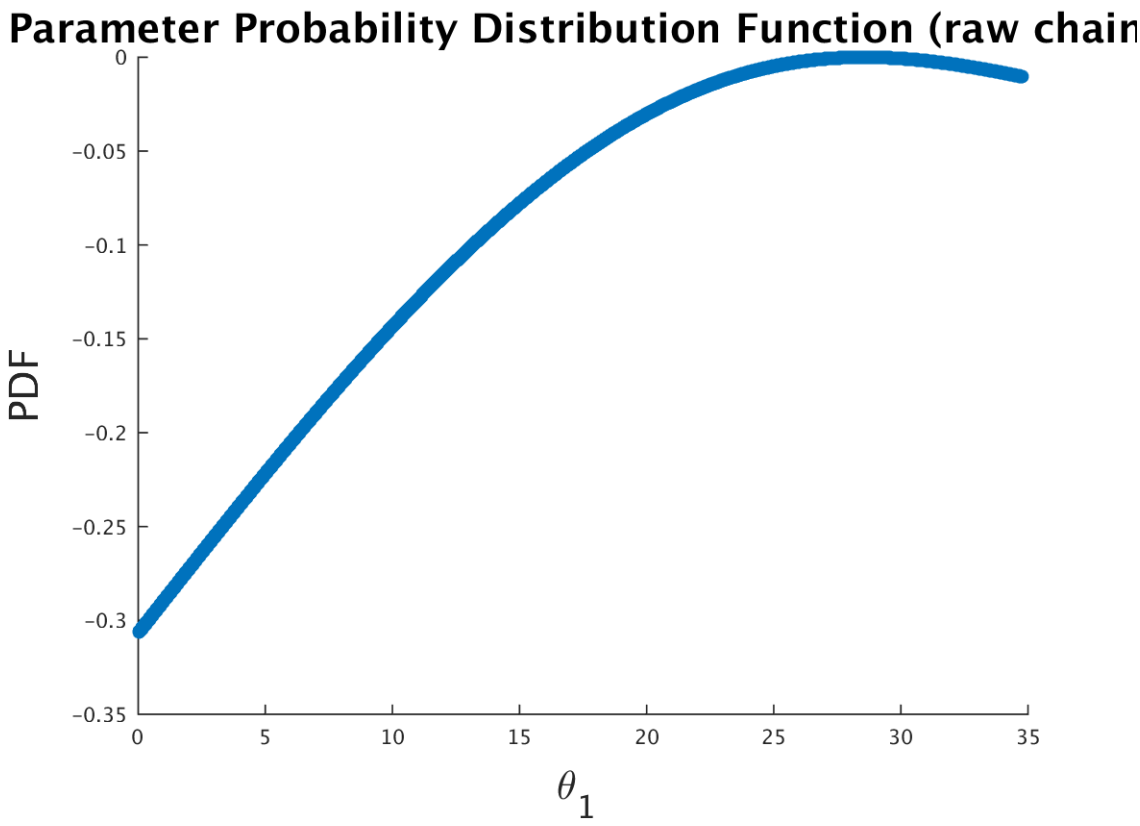

Figure 6.35: PDF function for Parameter

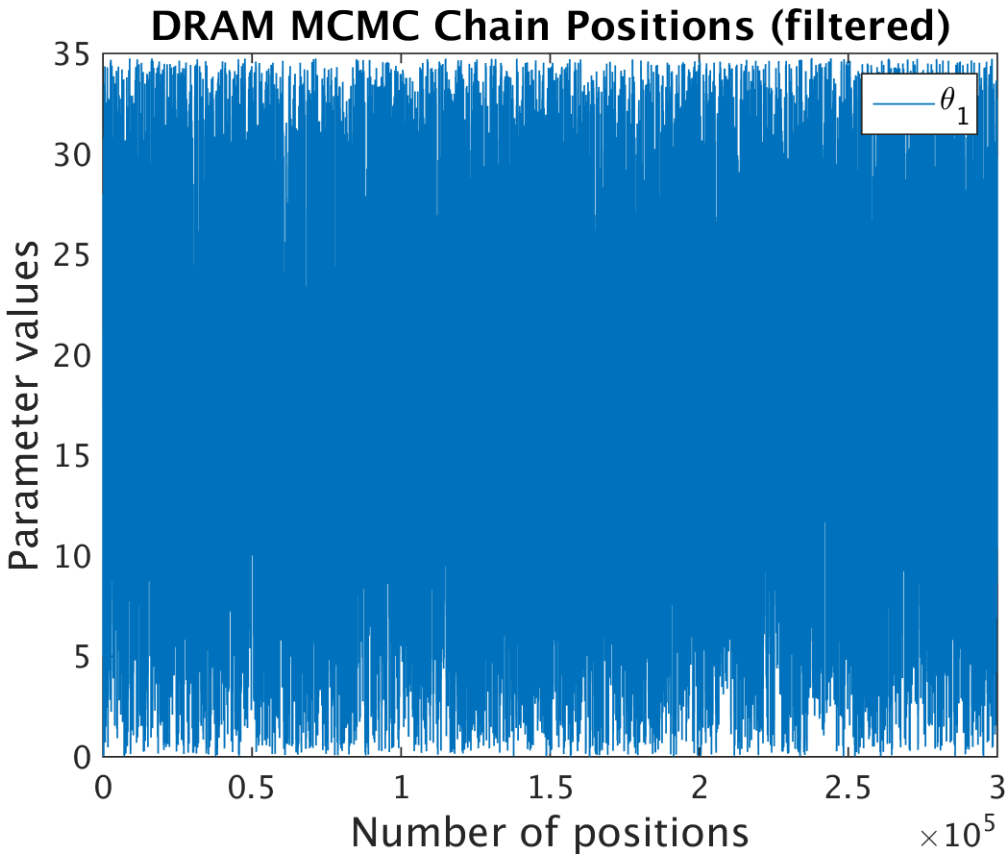

Figure 6.36: MCMC chain position

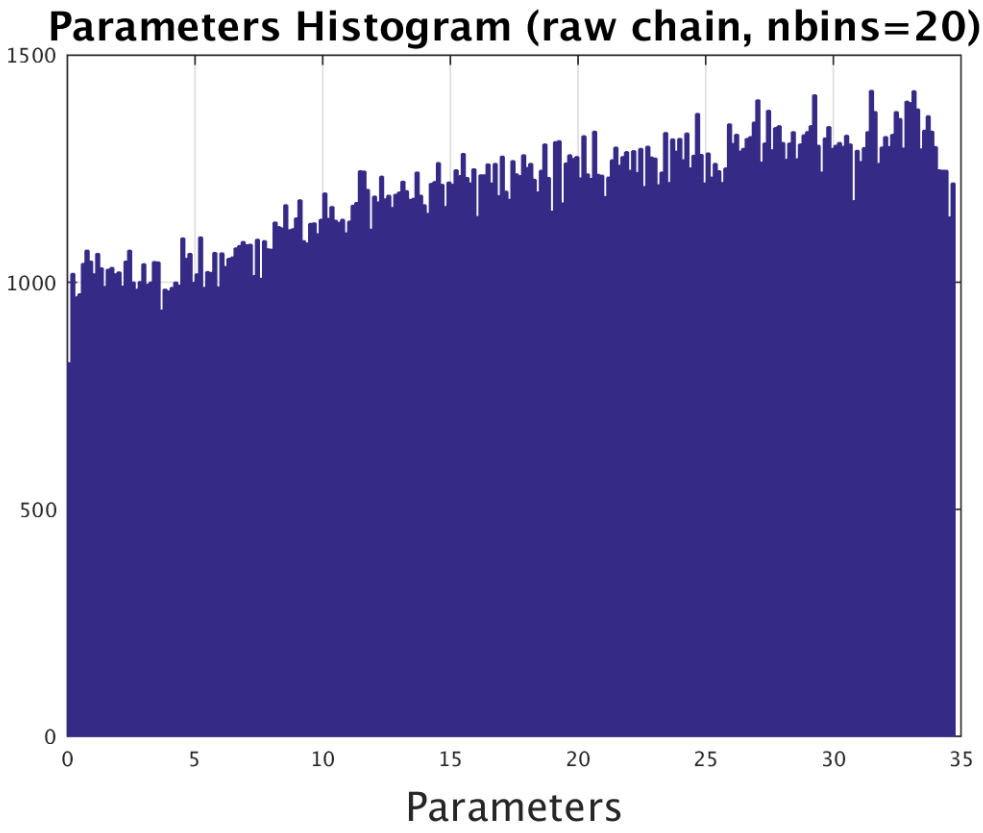

Figure 6.37: Histogram

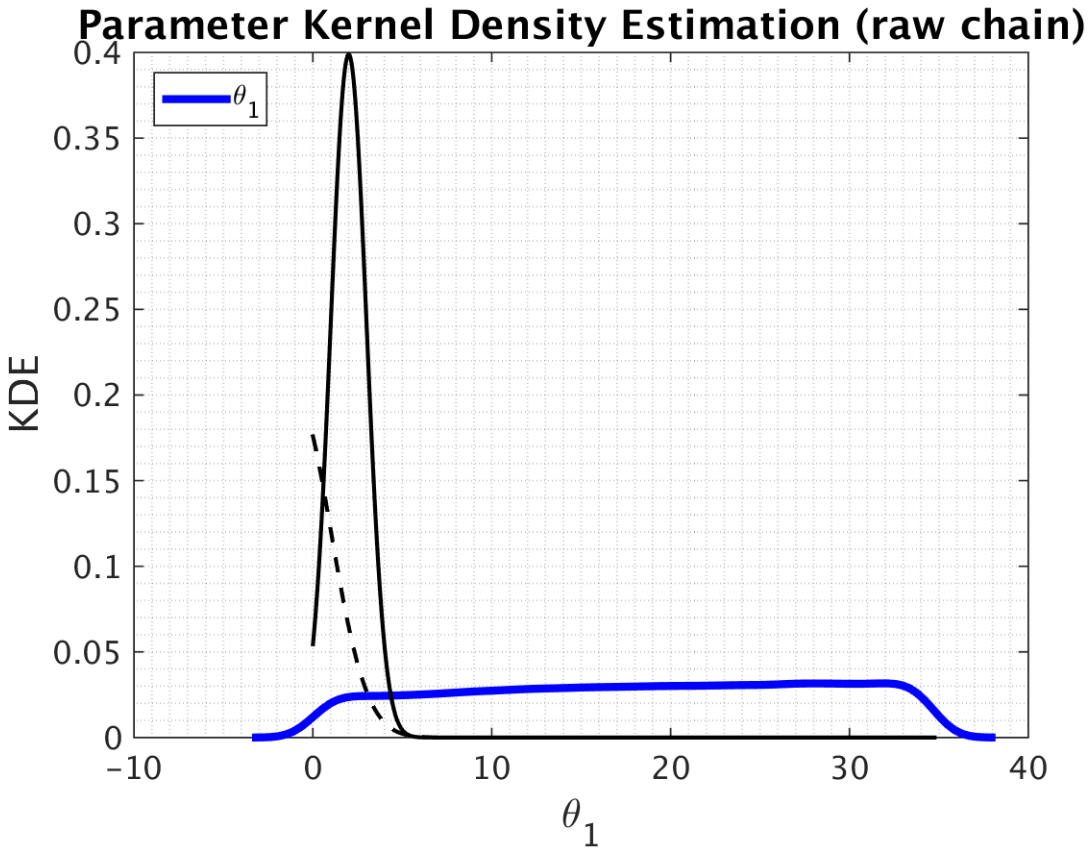

Figure 6.38: KDE

Chain size 700000

In this section we have chain size of 700000 points.

Chain size 900000

In this section we have chain size of 900000 points.

Chain size 1000000

In this section we have chain size of 1000000 points.

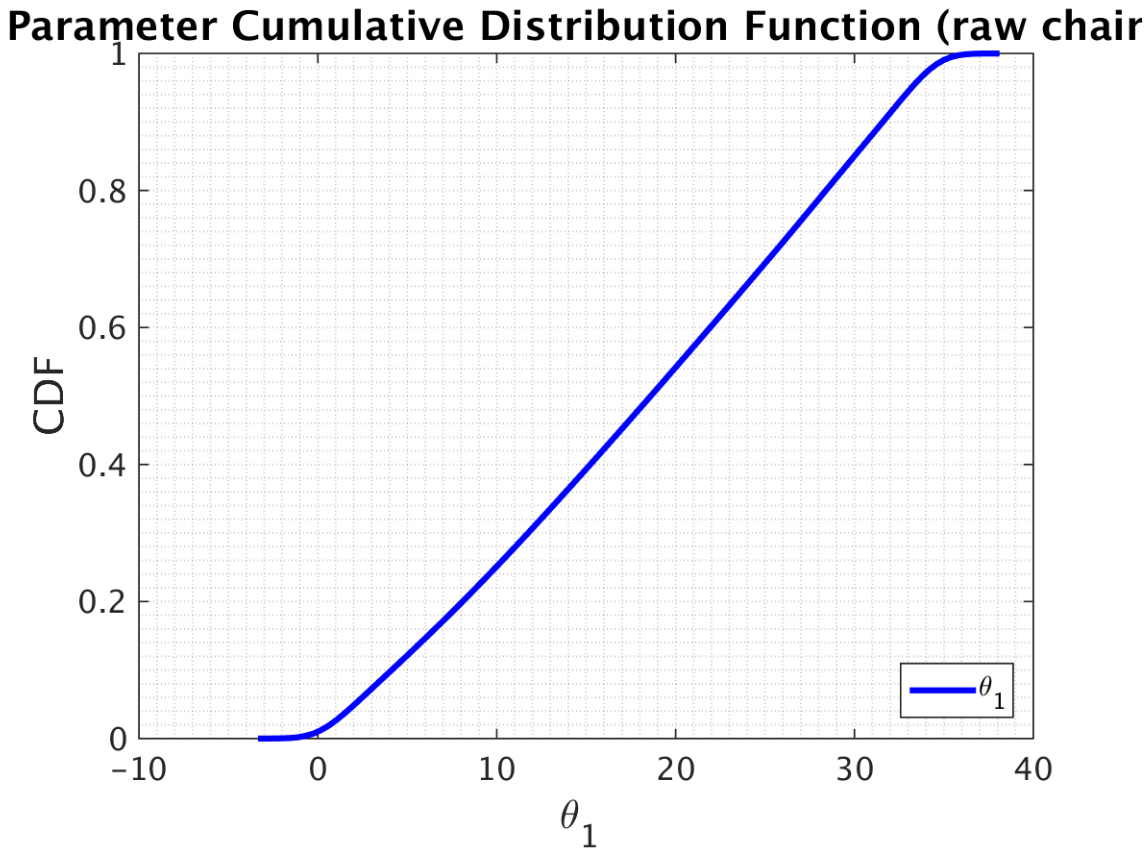

Figure 6.39: CDF function for Parameter

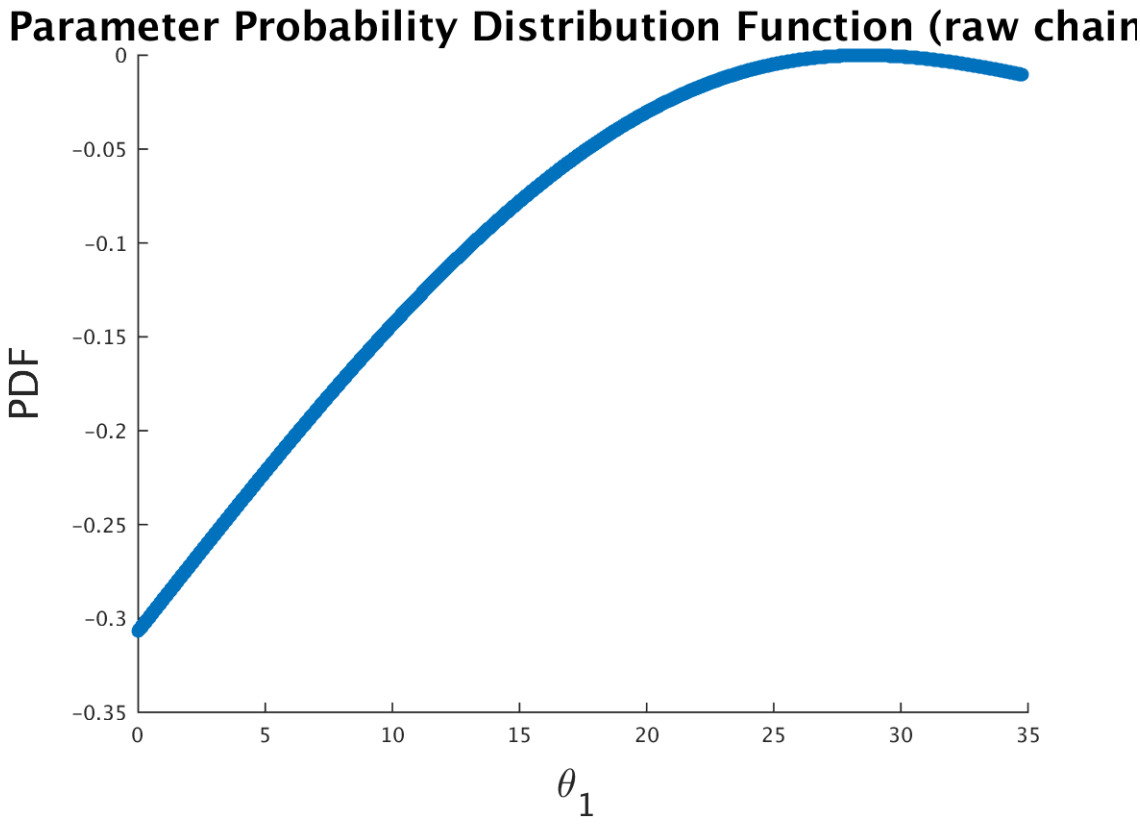

Figure 6.40: PDF function for Parameter

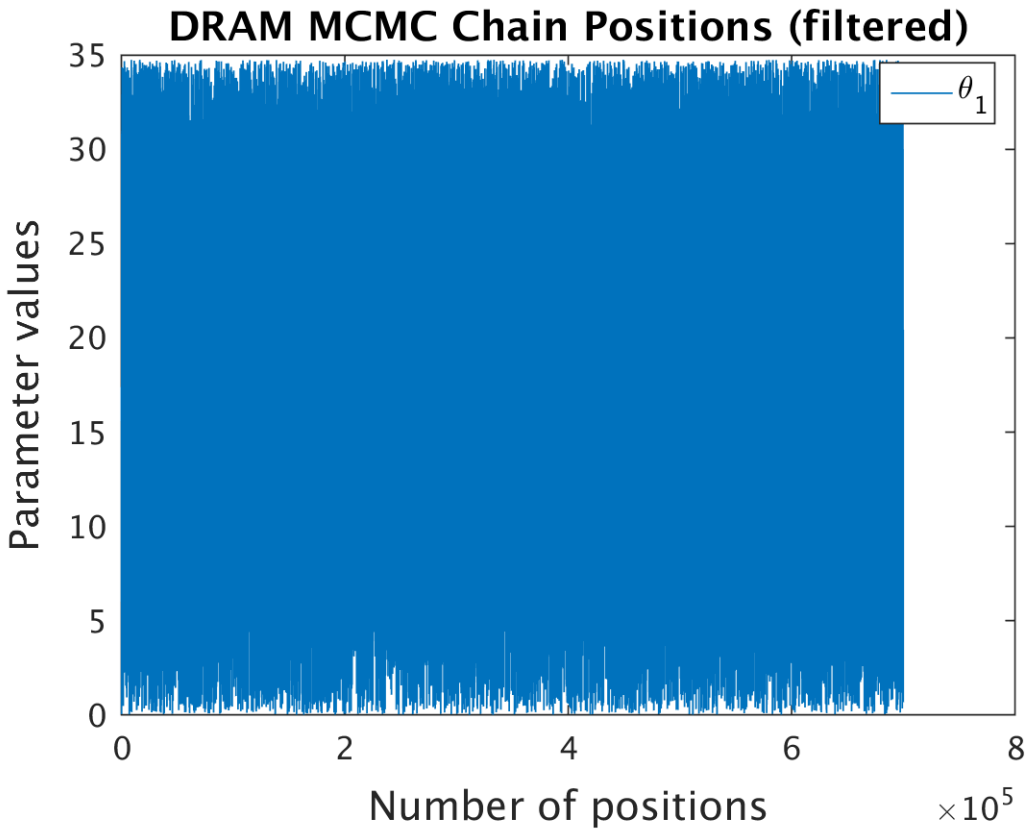

Figure 6.41: MCMC chain position

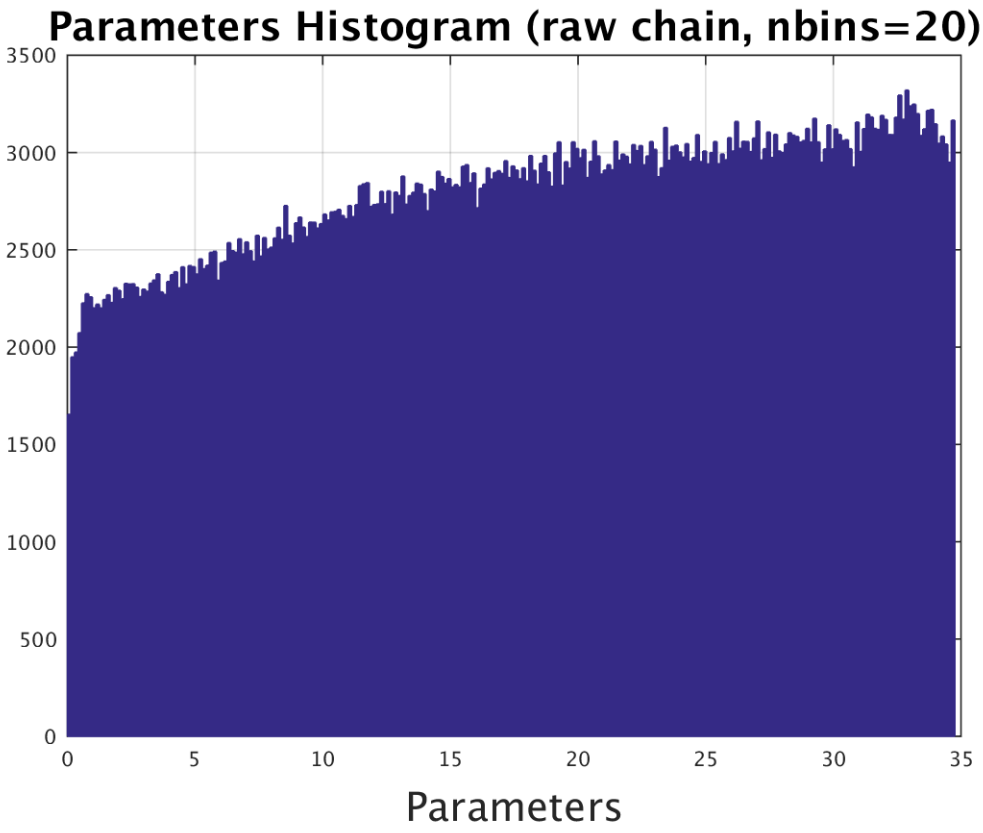

Figure 6.42: Histogram

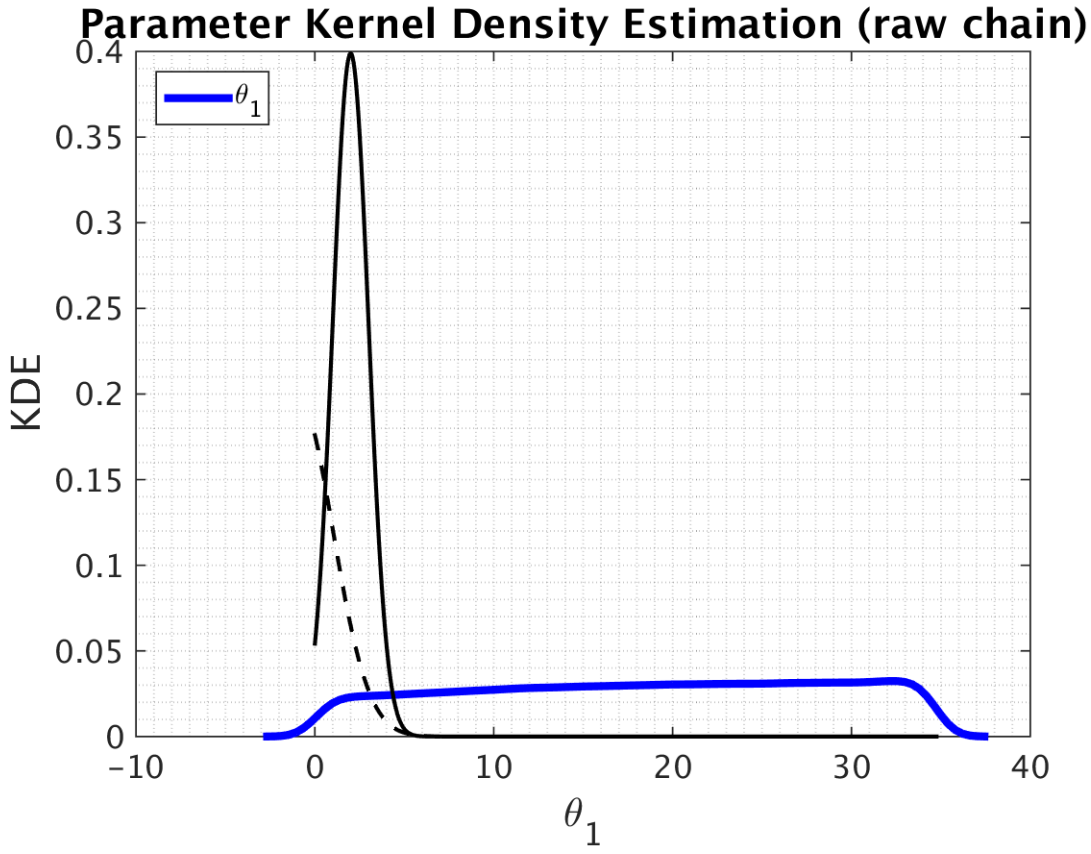

Figure 6.43: KDE

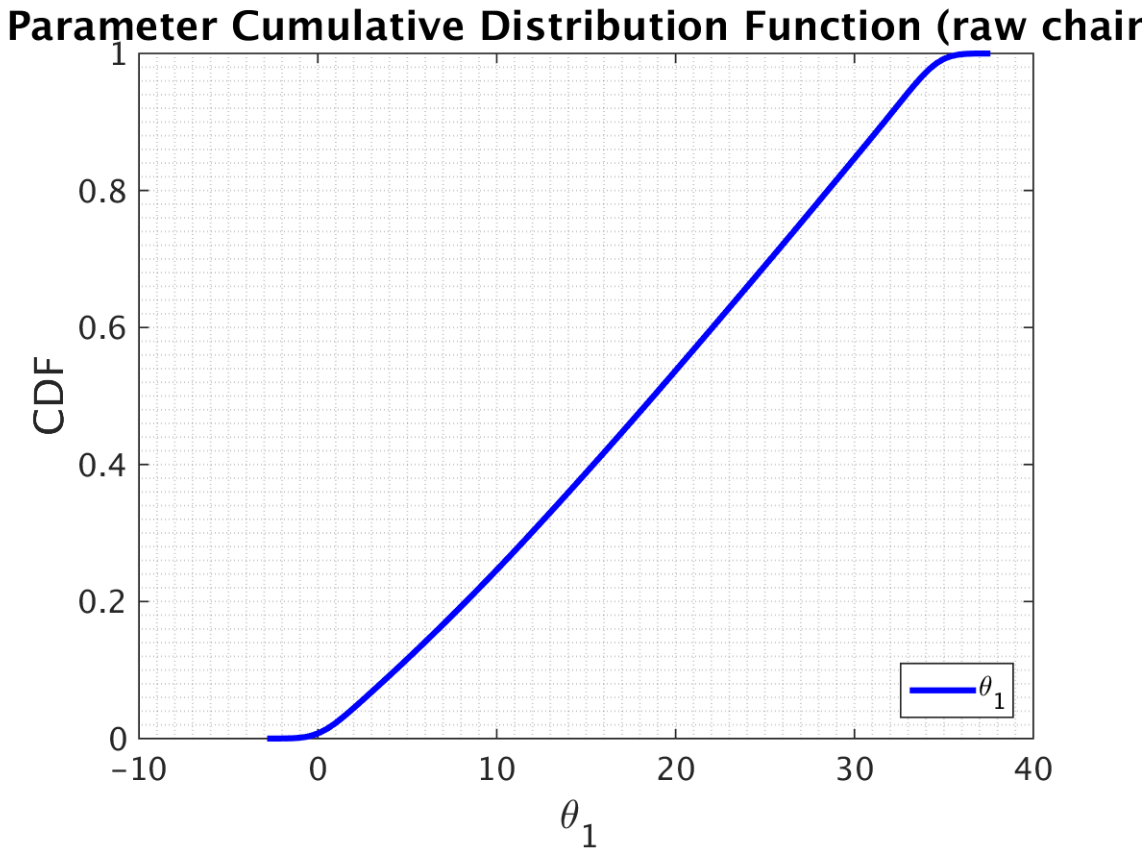

Figure 6.44: CDF function for Parameter

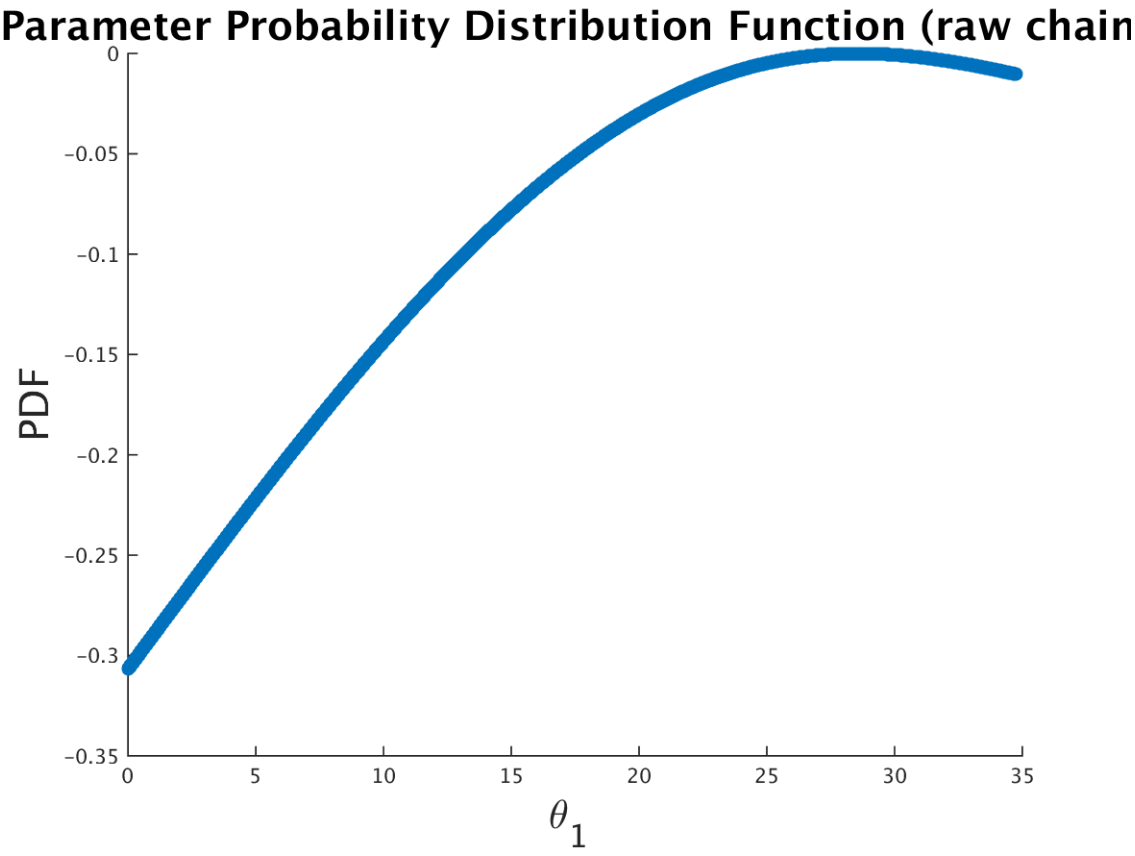

Figure 6.45: PDF function for Parameter

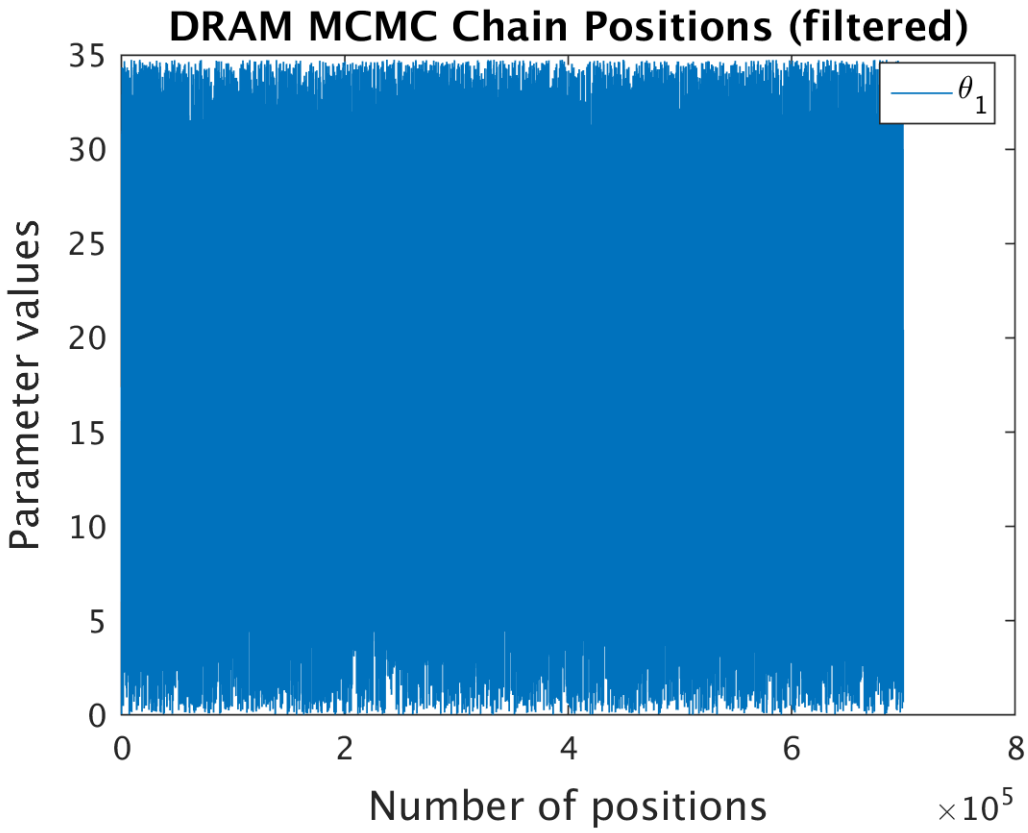

Figure 6.46: MCMC chain position

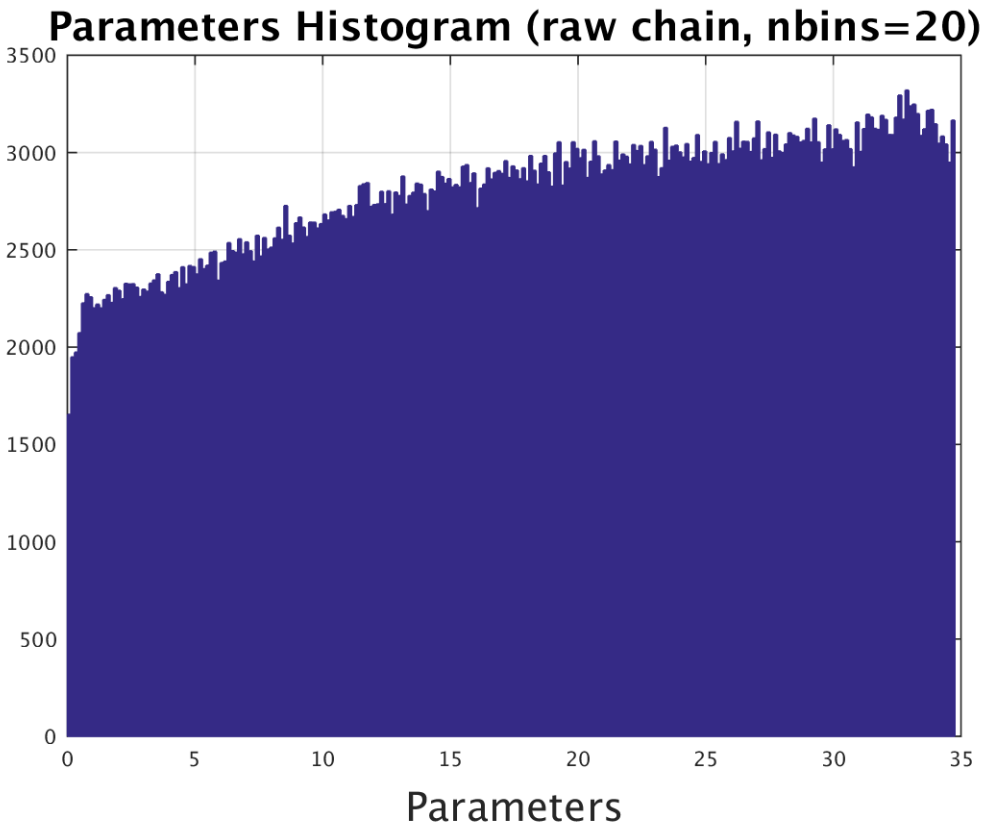

Figure 6.47: Histogram

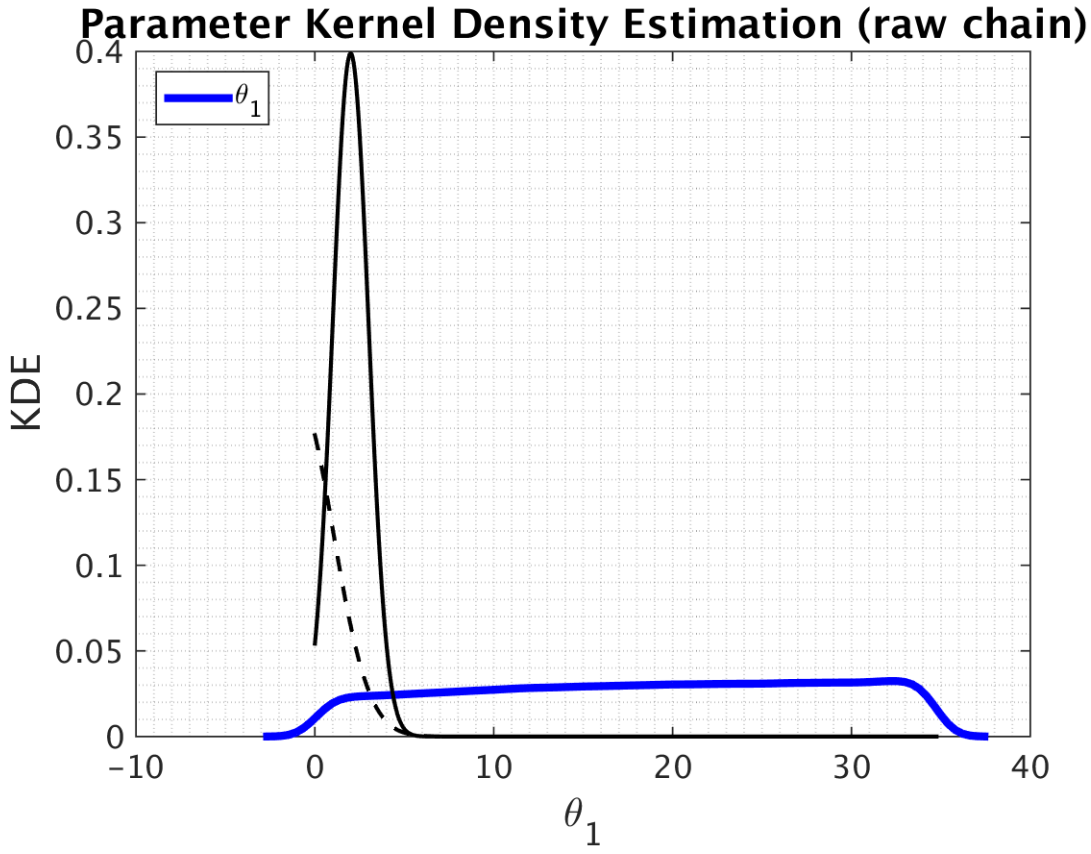

Figure 6.48: KDE

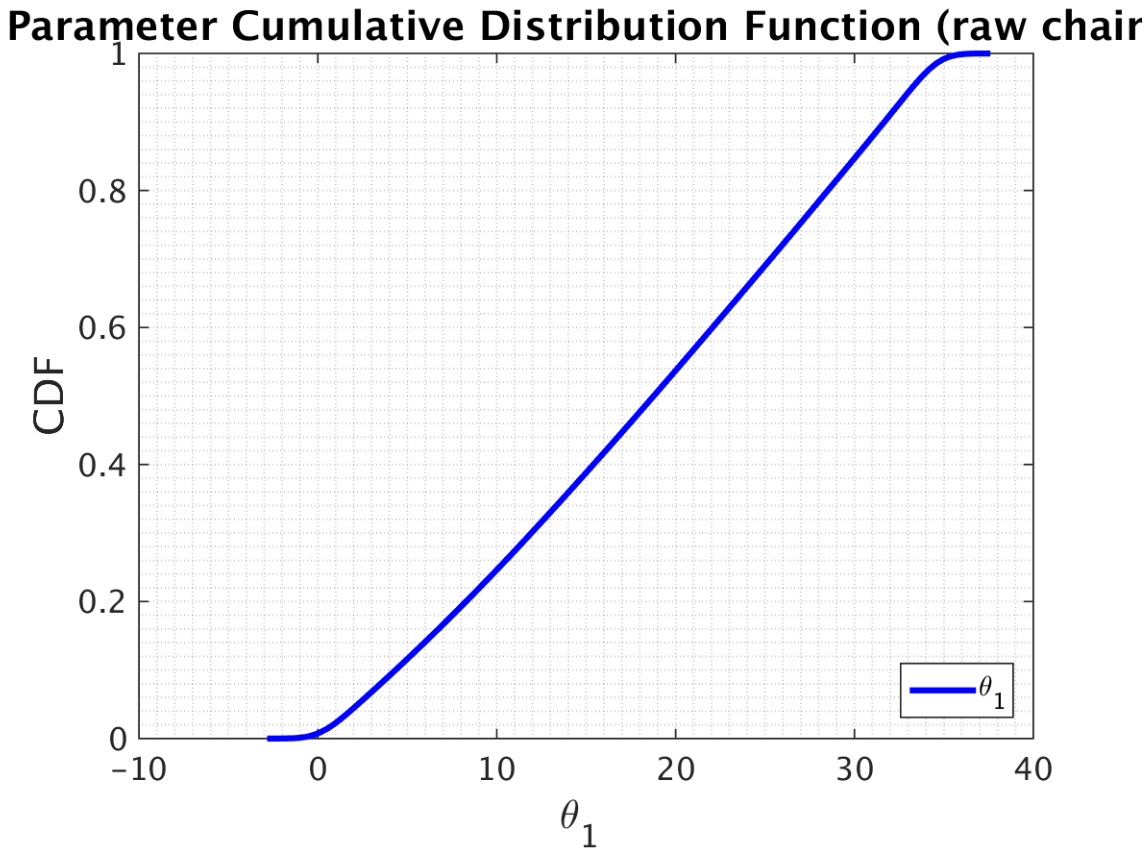

Figure 6.49: CDF function for Parameter

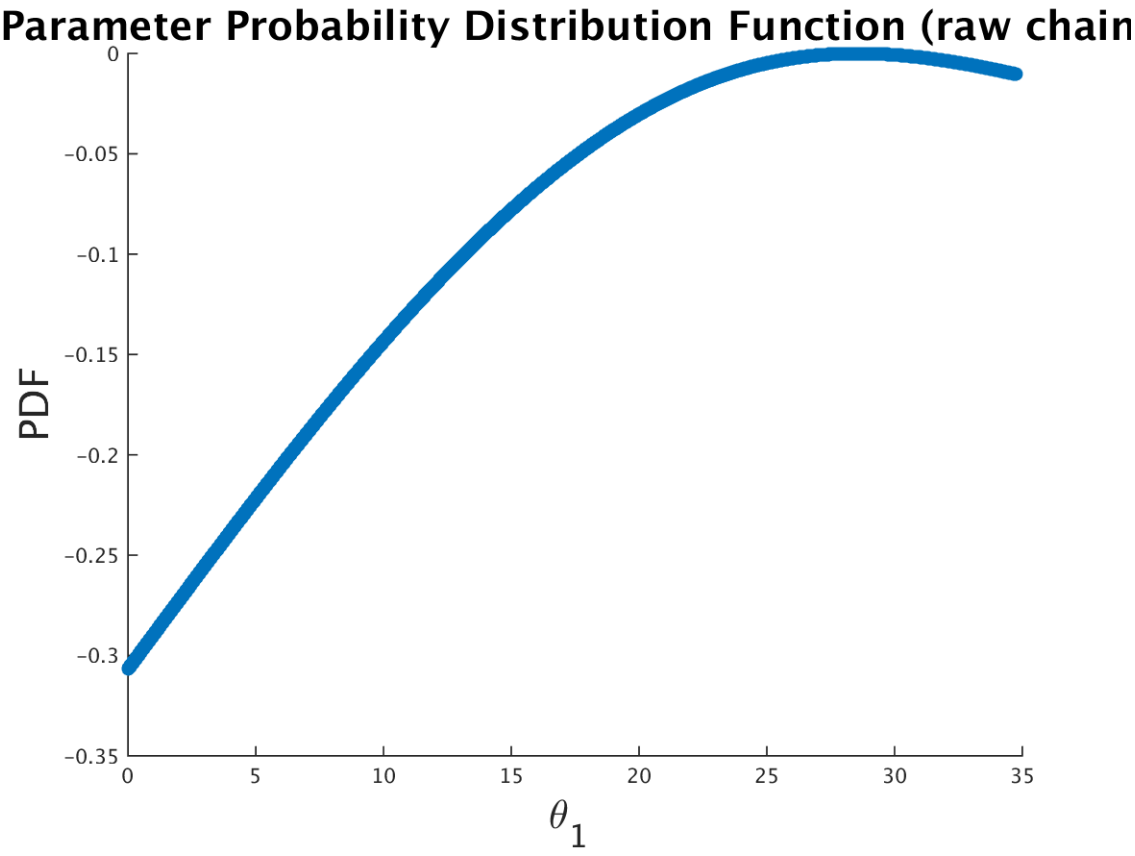

Figure 6.50: PDF function for Parameter

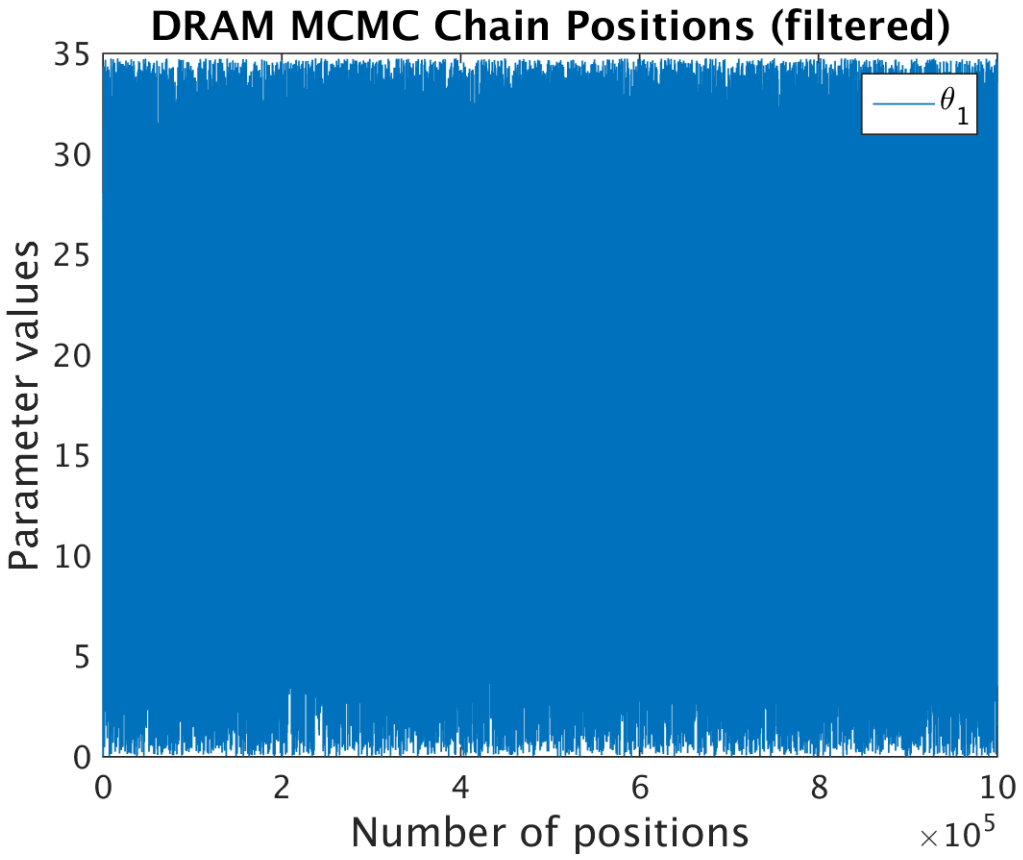

Figure 6.51: MCMC chain position

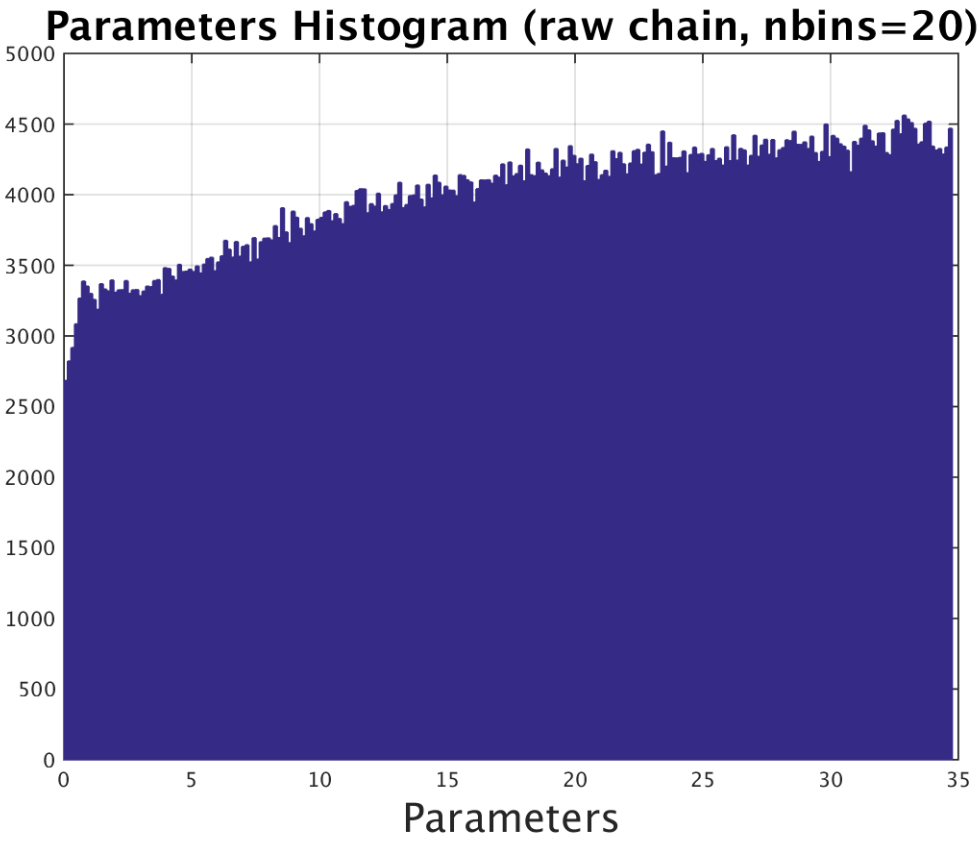

Figure 6.52: Histogram

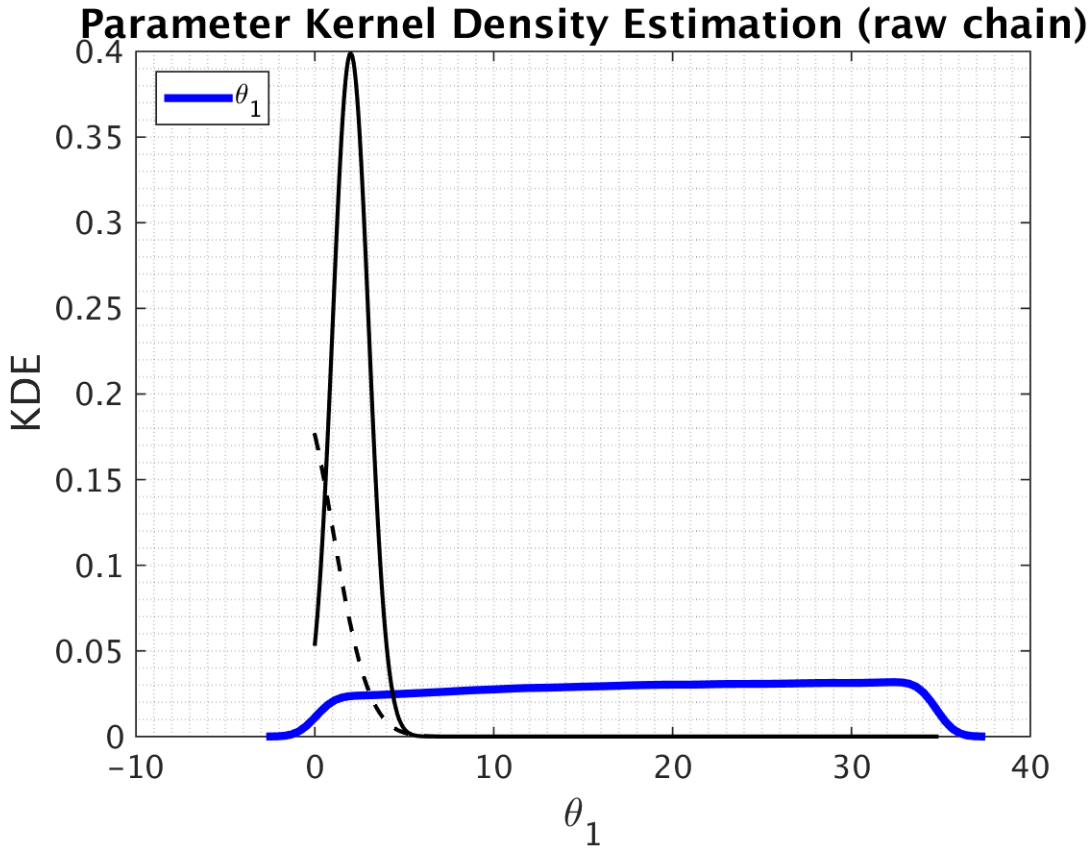

Figure 6.53: KDE

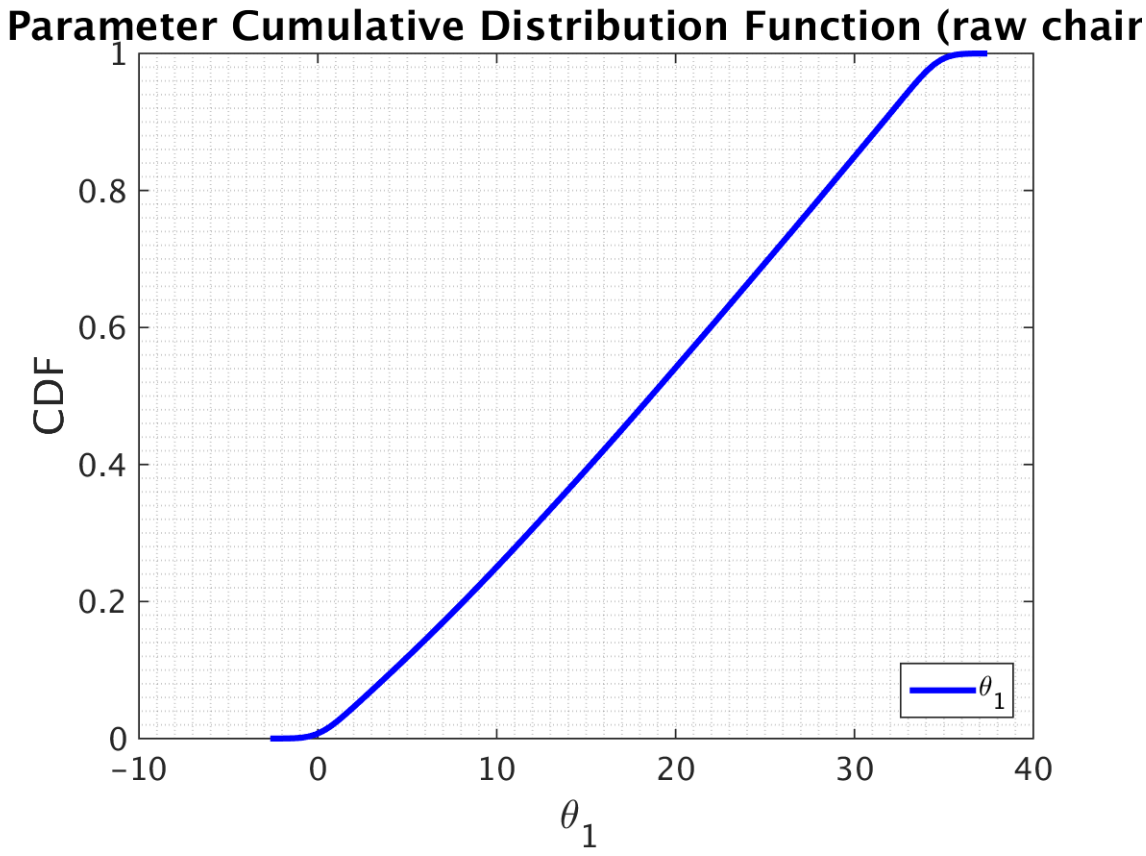

Figure 6.54: CDF function for Parameter

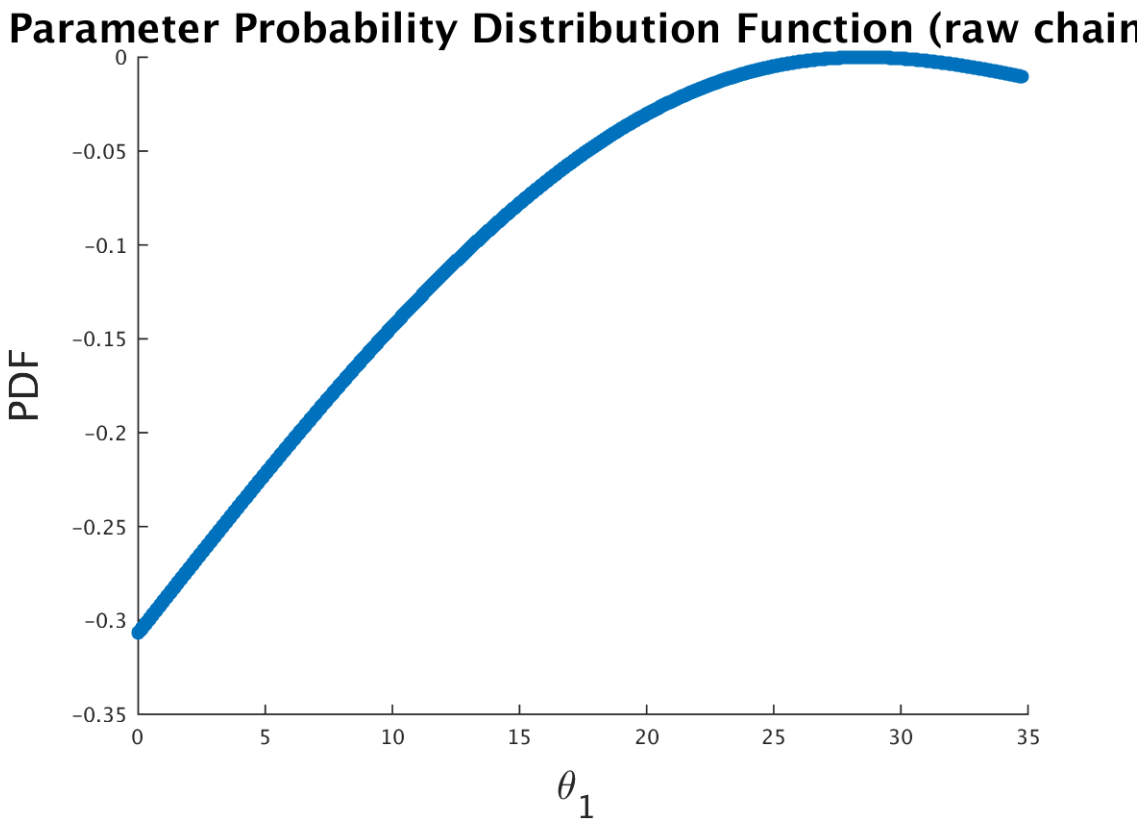

Figure 6.55: PDF function for Parameter

Chapter 7

Conclusion